

## Air Force Institute of Technology AFIT Scholar

---

Theses and Dissertations

Student Graduate Works

---

3-11-2011

# A Statistical Approach to Fusing 2-D and 3-D LADAR Systems

Paul F. Dolce

Follow this and additional works at: <https://scholar.afit.edu/etd>

Part of the [Optics Commons](#)

---

### Recommended Citation

Dolce, Paul F, "A Statistical Approach to Fusing 2-D and 3-D LADAR Systems" (2011). *Theses and Dissertations*. 1378.  
<https://scholar.afit.edu/etd/1378>

This Thesis is brought to you for free and open access by the Student Graduate Works at AFIT Scholar. It has been accepted for inclusion in Theses and Dissertations by an authorized administrator of AFIT Scholar. For more information, please contact [richard.mansfield@afit.edu](mailto:richard.mansfield@afit.edu).



A STATISTICAL APPROACH TO FUSING 2-D AND 3-D LADAR SYSTEMS

THESIS

Capt. Paul F. Dolce,

AFIT/GE/ENG/11-09

DEPARTMENT OF THE AIR FORCE  
AIR UNIVERSITY

**AIR FORCE INSTITUTE OF TECHNOLOGY**

Wright-Patterson Air Force Base, Ohio

APPROVED FOR PUBLIC RELEASE; DISTRIBUTION UNLIMITED.

The views expressed in this thesis are those of the author and do not reflect the official policy or position of the United States Air Force, Department of Defense, or the United States Government. This material is declared a work of the U.S. Government and is not subject to copyright protection in the United States.

AFIT/GE/ENG/11-09

A STATISTICAL APPROACH TO FUSING 2-D AND 3-D LADAR  
SYSTEMS

THESIS

Presented to the Faculty  
Department of Electrical and Computer Engineering  
Graduate School of Engineering and Management  
Air Force Institute of Technology  
Air University  
Air Education and Training Command  
In Partial Fulfillment of the Requirements for the  
Degree of Master of Science in Electrical Engineering

Capt. Paul F. Dolce, B.S.E.E.

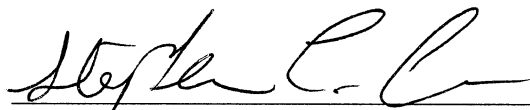
March 2011

APPROVED FOR PUBLIC RELEASE; DISTRIBUTION UNLIMITED.


A STATISTICAL APPROACH TO FUSING 2-D AND 3-D LADAR  
SYSTEMS

Capt. Paul F. Dolce, B.S.E.E.

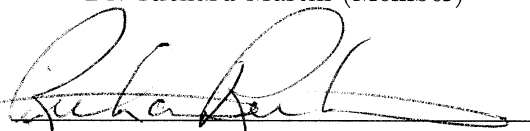
Approved:

  
\_\_\_\_\_  
Dr. Stephen Cain (Chairman)

22 Feb 2011  
date

  
\_\_\_\_\_  
Dr. Richard Martin (Member)

22 Feb 2013  
date

  
\_\_\_\_\_  
Mr. Rich Richmond (Member)

17 Feb 2011  
date

*Abstract*

LADAR (LAsER Detection and Ranging) systems can be used to provide 2-D and 3-D images of scenes. Generally, 2-D images possess superior spatial resolution due to the density of their focal plane arrays, but without range data. A 3-D LADAR system can produce range to target data at each pixel, but lacks the 2-D system's superior spatial resolution. The 3-D system is limited by its hardware, specifically its imaging array. Currently developers are investigating ways to change the pixel size in the 3-D LADAR imaging array, but the cost of this research is quite expensive and technically challenging. It is the goal of this work to develop an algorithm using an Expectation Maximization approach to estimate both range and the bias associated with a 3-D LADAR system. The algorithm developed demonstrates both spatial and range resolution improvement over standard interpolation techniques using both real and simulated 3-D and 2-D LADAR data.

## *Acknowledgements*

First and foremost, I would like to thank Dr. Stephen Cain, my academic and thesis advisor, for always being there when I needed guidance in Electro-Optics. His willingness to help me understand the subject made my time here at AFIT very enjoyable. The encouragement he gave me also helped to motivate my writings especially this thesis. There are many horror stories about thesis advisors at AFIT, but my experience with Dr. Cain was very much the opposite. I would be remiss without thanking my beautiful wife for her understanding and patience throughout my time at AFIT. She knew exactly when work needed to get done and kept my love for video games in check throughout my thesis writing. I cannot thank her enough for her willingness to keep me on schedule and on track. Finally, I would like to thank my fellow yeomen for helping me to get out of the house from time to time to relieve the stress of writing this document.

I dedicate this document to my family, especially my late grandmother. She has been my guiding angel throughout my life and it would only be right to dedicate my thesis to her and my family. Thanks grandma for always being there in spirit.

Capt. Paul F. Dolce

## Table of Contents

	Page
Abstract . . . . .	iv
Acknowledgements . . . . .	v
Table of Contents . . . . .	vi
List of Figures . . . . .	viii
List of Tables . . . . .	x
List of Abbreviations . . . . .	xi
I. Introduction . . . . .	1
1.1 Background . . . . .	1
1.2 Research Goals . . . . .	3
1.3 Assumptions . . . . .	3
1.4 Related Research . . . . .	3
1.4.1 Interpolation . . . . .	3
1.4.2 Microscanning . . . . .	4
1.4.3 Texture Mapping . . . . .	4
1.4.4 Blind Deconvolution . . . . .	4
1.5 Thesis Organization . . . . .	5
II. LADAR Sensor Model . . . . .	6
2.1 LADAR Sensor Models . . . . .	6
2.1.1 LADAR Hardware . . . . .	6
2.1.2 LADAR sensor models . . . . .	6
2.1.3 Simulated data . . . . .	10
2.1.4 Measured data . . . . .	13
III. Research Methodology . . . . .	18
3.1 Proposed Sensor Fusion Algorithm . . . . .	18
3.1.1 Formulating complete and incomplete data . . . . .	19
3.1.2 Finding the expectation . . . . .	20
3.1.3 Maximizing the Expectation . . . . .	22
3.2 Data Interpolation . . . . .	27
IV. Results and Analysis . . . . .	30
4.1 Simulated target results . . . . .	30
4.2 Measured data results . . . . .	33



	Page
V. Conclusions and Future Work . . . . .	38
5.1 Conclusions . . . . .	38
5.2 Future Work . . . . .	39
Bibliography . . . . .	40

## *List of Figures*

Figure		Page
2.1.	The components of a 3-D LADAR system while receiving a pulse.	7
2.2.	(a) The 50-by-50 target area. (b) The 13-by-13 raw estimated range from the undersampled 3-D data on the low resolution grid.	10
2.3.	2-D intensity images of the 3-D data cube over the course of 36 nanoseconds. Each image is shown on a 13-by-13 pixel grid and represents the data slice taken every 4 nanoseconds. . . . .	11
2.4.	(a) The low resolution (13-by-13) data slice. (b) The high resolution (50-by-50) data slice. (c) The 2-D data to be fused with the 3-D data. . . . .	12
2.5.	(a) 50-by-50 target area of the second simulation. (b) The 2-D image resulting from summing the second targets high resolution 3-D data cube. . . . .	13
2.6.	Setup to obtain measured data. . . . .	13
2.7.	Target area of measured data on a 64-by-64 grid. . . . .	15
2.8.	(a) The low resolution (16-by-16) data slice. (b) The high resolution (64-by-64) data slice. (c) The 2-D data that will be fused with the 3-D data. . . . .	16
2.9.	2-D intensity images of the 3-D measured data cube. Each image is shown on a 16-by-16 pixel grid. . . . .	17
3.1.	(a) 32-by-32 sample image. (b) Comb of the sample image on a 128 pixel grid. . . . .	28
4.1.	Range RMSE vs iterations after applying the proposed algorithm to the first target. This graph shows the RMSE reducing drastically between zero and fifty iterations. Due to the steady tail of the data, more than 400 iterations of the algorithm would only make minor reductions in RMSE of the range. . . . .	31
4.2.	(a) 50-by-50 range truth of the first target. First target 50-by-50 estimated ranges: (b) Pixel replication estimated range. (c) Linear estimated range. (d) Cubic estimated range. (e) EM algorithm's estimated range. . . . .	32

Figure		Page
4.3.	Range RMSE vs iterations after applying the proposed algorithm to the second target. This graph shows a great reduction in RMSE happening between zero and approximately seventy-five. The algorithm reached approximate convergence at a slower rate for this target as compared to the first target. . . . .	34
4.4.	(a) 50-by-50 2-D range truth of the second target. Second target 50-by-50 2-D estimated ranges: (b) Pixel replication estimated range. (c) Linear estimated range. (d) Cubic estimated range. (e) EM algorithm's estimated range. . . . .	35
4.5.	Range RMSE vs iterations after applying the proposed algorithm to the measured data. The graph shows the most RMSE reduction occurring between zero and forty iterations. The algorithm reaches convergence after approximately the hundredth iteration.	36
4.6.	(a) 40-by-40 3-D range truth of the measured data. Measured data 40-by-40 3-D estimated ranges: (b) Pixel replication estimated range. (c) Linear estimated range. (d) Cubic estimated range. (e) EM algorithm's estimated range. . . . .	37

*List of Tables*

Table		Page
4.1.	Method comparison for the first target . . . . .	33
4.2.	Method comparison for the second target . . . . .	33
4.3.	Method comparison for the measured data . . . . .	36

*List of Abbreviations*

Abbreviation		Page
LADAR	LAser Detection and Ranging . . . . .	1
USAF	United States Air Force . . . . .	1
EM	Expectation Maximization . . . . .	3
PSF	point spread function . . . . .	3
OTF	optical transfer function . . . . .	7
RMSE	root mean square error . . . . .	30

# A STATISTICAL APPROACH TO FUSING 2-D AND 3-D LADAR SYSTEMS

## I. Introduction

This chapter describes the problem to be addressed by this research. The background of the problem and goals for this research are given, as well as assumptions used to limit the scope of the research. A discussion of previous related research is provided as well as the organization for the rest of the thesis.

### 1.1 Background

FLASH 3-D *LA*ser *De*tecti*o*n and *R*ang*i*ng (LADAR) systems represent an important advancement in imaging technology in that they capture an entire scene simultaneously as opposed to the way scanning systems form imagery. 3-D FLASH systems suffer from spatial resolution problems due to pixel pitch fabrication limitations. A 2-D system can produce high spatial resolution images but without range data. The 3-D system can produce range to target data, but lacks the 2-D system's superior spatial resolution. The 3-D system is limited by its hardware, specifically its imaging array's pixel pitch. Pixel pitch is the distance between each pixel in an array. The pixel pitch of many 3-D systems is 100 micro-meters while the 2-D system possesses a pixel pitch of 10 or 25 micro-meters. Currently developers are investigating ways to improve the pixel size in the 3-D LADAR imaging array, but the costs of this research is quite expensive and technically challenging.

Obtaining better spatial resolution from a 3-D LADAR system would improve LADAR systems with potential *United States Air Force* (USAF) LADAR applications. Some defensive systems use LADAR for navigation, target recognition, and reconnaissance. Currently researchers are trying to develop LADAR systems that help autonomous vehicles navigate around unfamiliar terrain. One technology allows

a 3-D LADAR system to communicate with a vehicles inertial measurement unit to provide motion estimates to the vehicle using absolute orientation [6]. Collections of these motion estimates provide navigation to the vehicle as well as other systems.

Automatic target recognition is a big focus for the USAF. This type of technology opens up the use of loitering munitions, munitions' miniaturization, and target recognition. In 2007 Lockheed Martin developed a LADAR based seeker head for target recognition, known as E-LADAR [13]. This technology improves the accuracy of many munitions, which improves the lethality of force and decreases collateral damage of the munitions. Pilots also use target recognition, a 3-D target image allows them to make better decisions to discern a target from a non-target. Improvement of the system's range estimation would make it more accurate and would increase the munitions resolution of a target.

Intelligence plays a big role in today's battlefield; knowing where to go and the location of the enemy are keys to maintaining dominance of a battlefield. Reconnaissance by LADAR can create 3-D maps of whole scenes on the ground from airframes. After the aerial LADAR data is collected terrain maps are developed which aid change detection in battlefield environments. Commanders use the 3-D terrain maps in conjunction with other intelligence to develop battle plans or investigate adversaries. Improving both range estimation and spatial resolution of a 3-D LADAR system would allow autonomous vehicles to fly closer to targets and through urban areas, create pinpoint accuracy for munitions, and improve battlefield intelligence as well as air and space dominance.

One method for obtaining better spatial and range resolution from 3-D LADAR systems is to interpolate the images through various techniques. While this may suffice as a solution to the 3-D pixel size problem, it is not as accurate in reference to spatial and range resolution of the 3-D images. Interpolation may introduce errors due to aliasing effects.

## 1.2 *Research Goals*

The primary goal of this research is to prove that fusing both 2-D and 3-D LADAR images through *Expectation Maximization* (EM) will increase the spatial and range accuracy of the 3-D system.

## 1.3 *Assumptions*

For this research, the following assumptions were made:

- The LADAR pulse returns exist within the range gate of the system
- The total LADAR system *point spread function* (PSF) stays fixed and is known or can be measured
- The LADAR location is known in simulated data
- The 2-D and 3-D LADAR system's images are pre-registered and aligned

## 1.4 *Related Research*

This section describes other methods to improve 3-D LADAR resolution and range estimation. The methods discussed are interpolation, microscanning, texture mapping, and blind deconvolution.

*1.4.1 Interpolation.* Interpolation is a method in which new data points are created from a set of sampled data points. Data interpolation can be done in numerous ways, for the purpose of this work we will focus on the pixel replication (zero-order), linear (first-order), and cubic interpolators. An interpolator takes the data given to it and creates new data to a desired range. The new data created is an approximation based on surrounding information. Through image interpolation, each pixel and its surrounding pixels are used to determine the new pixels. This smoothes the data out and allows one to expand the resolution of an image. Interpolating the data is a quick process and is a standalone method. The interpolators only rely on the 3-D LADAR data and they do not take into account the 2-D LADAR data. These



attributes make data interpolation an attractive method for extracting information from the 3-D LADAR system. Interpolation does not reduce aliasing that already exists in an image [8].

*1.4.2 Microscanning.* Microscanning is a method that involves registering numerous 3-D LADAR data cubes in every dimension. It has been proven to increase spatial resolution and reduce range estimation error of 3-D LADAR systems. The microscanning process registers the images of all the data cubes at sub-pixel resolution and then uses interpolation to estimate the range of the target [1]. While under some circumstances microscanning may suffice, the system can have some latency, due to waiting on the many frames it requires. If the target ends up changing during the microscanning process, frames could get misregistered and ultimately produce an unwanted image. The algorithm proposed takes a single 3-D data cube and improves its spatial resolution and range accuracy.

*1.4.3 Texture Mapping.* Texture mapping is the process of taking high resolution 2-D images and overlaying them onto 3-D LADAR scenes or aerial stereo imaging. This method improves the way 3-D images aesthetically look but does not improve the range accuracy [5]. The method registers the 2-D image with a 3-D scene and wraps the 2-D image around the 3-D scene. The data fusion proposed in this research is very different from texture mapping. The data fusion proposed uses statistics to estimate ranges based on both 3-D and 2-D images.

*1.4.4 Blind Deconvolution.* There are two previous research efforts that used blind deconvolution to improve 3-D LADAR range estimation, McMahan's [7] and Cain's [2] both use a blind deconvolution method. Cain's blind deconvolution method was developed strictly using the Richardson-Lucy algorithm to estimate the pulse shape and then extract the range from the shape. Cain's work did not estimate the intensity of the signals and assumed it was known. McMahan's work is similar, it uses the EM process to come up with an algorithm to estimate pulse shape and

extract the range from it. McMahon's work deals with critically sampled data. The data used in this study has been aliased to properly set up a case for 3-D LADAR systems, e.g. munitions' seekers, machine vision, etc. The proposed algorithm also estimates the range directly without extracting it from the pulse shape.

### ***1.5 Thesis Organization***

*Chapter II* provides a description of the LADAR sensor model and data development used for this research. *Chapter III* explains the mathematical derivation of the algorithm and methodology of the research. *Chapter IV* details the results from the simulations described in *Chapter III*. Finally, *Chapter V* gives a summary of the research and lists conclusions of the thesis as well as potential follow-on research areas.

## II. LADAR Sensor Model

This chapter provides the technical background necessary for understanding the overall concepts of this research. A description of the LADAR sensor model is provided and describes how data was developed for this work.

### 2.1 LADAR Sensor Models

2-D and 3-D LADAR systems interrogate scenes through optics as well as the atmosphere using laser pulses. Models exist for each system that relate the target plane coordinates  $(x, y)$ , to the system's focal array plane coordinates  $(u, v)$ . The coordinates represent pixels in the arrays. The following subsections will describe the sensor models and how the data was developed for this work.

*2.1.1 LADAR Hardware.* Before discussing the details of modeling a FLASH LADAR system one must understand its hardware. Most 3-D FLASH LADAR systems contain the same components as shown in figure 2.1. When a scene is shot, the laser transmits through a diffuser (beam spreader) in order to cover the area of the scene. The lasers clock rate determines the pulse width of the laser. In this research, the pulse width of the measured data is 2.5 nanoseconds. Using the diffuser ensures uniform illumination of the target. Once the beam hits the target, the beam reflects off the target creating a return pulse back to the system. This pulse is put through lensing that sizes the pulse down to the focal array (array of receivers). Focal array sizes vary from system to system. The light hitting the focal array goes through a data processor that determines the ranges contained in the scene shot. The processed data then becomes the 3-D scene of the target.

*2.1.2 LADAR sensor models.* A 2-D LADAR system produces 2-D intensity image of a target. Most 2-D systems can achieve a 25 micrometer or smaller pixel pitch which can produce high resolution intensity images. The intensity received from the target is not the same as the intensity of the target. A relationship exists between target intensity and the received intensity in the focal plane and is shown in

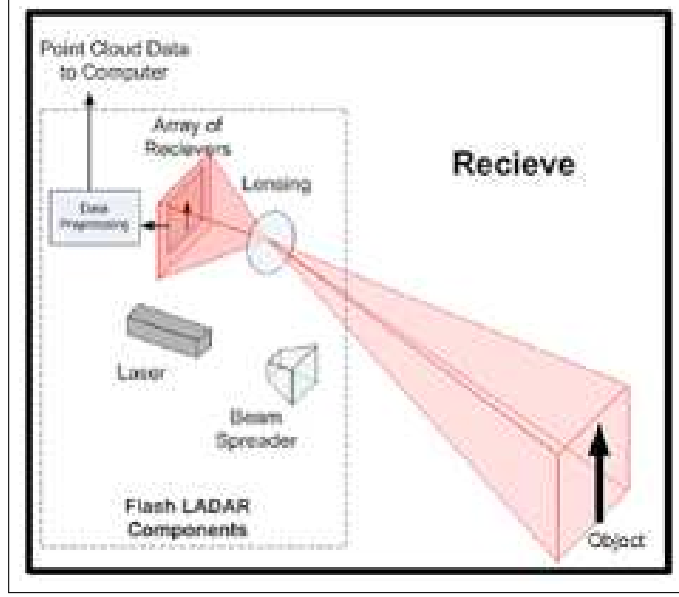


Figure 2.1: The components of a 3-D LADAR system while receiving a pulse.

Eq. (2.1) [2]. The target intensity is  $A(x, y)$ , and the focal plane intensity is  $i(u, v)$ .  $N$  is the number of pixels in the high-resolution image plane in each dimension.

$$i(u, v) = \sum_{x=1}^N \sum_{y=1}^N A(x, y) h(u - x, v - y) \quad (2.1)$$

Equation (2.1) is a convolution of the target intensity with the PSF,  $h(x, y)$ . This intensity model is used to find the intensity of an incoherent system [4]. The LADAR laser light is coherent in nature, but its detected light return is modeled as incoherent therefore the use of Eq. (2.1) is justified.

The PSF represents the effects of all the optics as well as the atmosphere. The *optical transfer function* (OTF) of the optics,  $H_{opt}(f_x, f_y)$ , is the effect the optics have on the pulse or lightwave coming through the system.  $H_{opt}(f_x, f_y)$  can easily be found by autocorrelating the pupil function ( $t_{lens}$ ) as shown in Eq. (2.3) [4]. The variables  $(f_x, f_y)$  represent the spatial frequencies in two dimensions.

$$t_{lens}(x, y) = \begin{cases} 1, & \text{for } (x, y) \text{ in the aperture} \\ 0, & \text{for } (x, y) \text{ outside the aperture} \end{cases} \quad (2.2)$$

$$H_{opt}(f_x, f_y) = \frac{\sum_{x=1}^J \sum_{y=1}^J t_{lens}(x + \frac{\lambda f_l f_x}{2}, y + \frac{\lambda f_l f_y}{2}) t_{lens}(x - \frac{\lambda f_l f_x}{2}, y - \frac{\lambda f_l f_y}{2})}{\sum_{x=1}^J \sum_{y=1}^J |t_{lens}(x, y)|^2} \quad (2.3)$$

The variable  $\lambda$  represents the laser wavelength and  $f_l$  is the focal length of the system.  $J$  represents the number of pixels in each dimension of a system's pupil.  $H_{opt}(f_x, f_y)$  may have range dependency but for this research it will stay fixed for simplicity. The atmospheric OTF,  $H_{atm}(f_x, f_y)$ , is an average and is found using Eq. (2.4) [10]. The equation represents the average effects of the atmosphere through short exposure. The equation uses the wavelength of the laser, the focal length of the system, Fried's seeing parameter ( $r_o$ ), and diameter of the lens ( $D_r$ ). Fried's seeing parameter is formed by weak and strong atmospheric turbulence. A high  $r_o$  will dictate weak turbulence, while strong turbulence is represented by a small  $r_o$ .

$$H_{atm}(f_x, f_y) = e^{-3.44 \left[ \frac{\lambda^2 f_l^2 (f_x^2 + f_y^2)}{r_o^2} \right]} \left\{ 1 - \left[ \frac{\lambda^2 f_l^2 (f_x^2 + f_y^2)}{D_r^2} \right] \right\} \quad (2.4)$$

There is also spatial blurring that is caused by each detector due to most images being bigger than a single detector. This blurring has its own transfer function  $H_{det}(f_x, f_y)$ .  $H_{det}(f_x, f_y)$  is created from taking the Fourier transform of a 2-by-2 rect function which is a sinc function. Multiplying the optics' OTF, atmospheric OTF, and the detector transfer function creates  $H_{tot}(f_x, f_y)$  (Eq. (2.5)) in the Fourier domain. Taking the inverse Fourier transform of  $H_{tot}(f_x, f_y)$  results in the PSF,  $h(x, y)$ .

$$H_{tot}(f_x, f_y) = H_{det}(f_x, f_y) H_{atm}(f_x, f_y) H_{opt}(f_x, f_y) \quad (2.5)$$

The pulses from the 3-D LADAR system will be modeled as Gaussian in time as shown in Eq. (2.6). By keeping  $A(x, y)$  fixed the 3-D pulse becomes a function of the range at each pixel,  $r(x, y)$ . The variable  $r_k$  represents discrete ranges each time the pulse is sampled by the 3-D system, for each sample a 2-D image is made which combine to make a 3-D image. The variable  $\sigma$  is the pulse width in meters.

$$P(x, y, r_k) = \frac{A(x, y)}{\sqrt{2\pi\sigma}} e^{-\frac{(r_k - r(x, y))^2}{2\sigma^2}} \quad (2.6)$$

The 3-D data's focal plane intensity is found by convolving the PSF,  $h(x, y)$ , and the pulse as shown in Eq. (2.7). Equation (2.7) also contains the bias,  $B(u, v)$ , that is present in the measured data. The bias is generated is a result of dark current added to the signal. This research assumes that the bias follows a Poisson distribution due to its discrete nature [7].  $L$  is the under sampling factor between the 2-D and 3-D data. The pixel pitch of each system determines the undersampling factor.

$$I(u, v, r_k) = \sum_{x=1}^N \sum_{y=1}^N P(x, y, r_k) h(Lu - x, Lv - y) + B(u, v) \quad (2.7)$$

The 3-D data ( $d(u, v, r_k)$ ) is a Poisson random variable with a mean of  $I(u, v, r_k)$ . The 3-D data model was chosen because incoherent light can be modeled as a Poisson random variable. The LADAR laser light is coherent which makes the modeling of the system robust. The choice to treat the laser light as incoherent light is based on the success of previous works modeling the LADAR light as incoherent [7], [2]. Assuming every pixel and every time instance in the 3-D data is independent the joint probability ( $p(d)$ ) of the data is shown in Eq. (2.8). The variable  $M$  is number of pixels in the 3-D image plane (low resolution plane) in each dimension and has the relationship  $M = \frac{N}{L}$ . The variable  $K$  represents the total number of 2-D images contained in the 3-D data. Summing the all the images contained in the 3-D data creates the 2-D images that will be used for the data fusion. The subsections below discuss the two types of data used in this work.

$$p(d) = \prod_{u=1}^M \prod_{v=1}^M \prod_{k=1}^K \frac{I(u, v, r_k)^{d_2(u, v, r_k)} e^{-I(u, v, r_k)}}{d_2(u, v, r_k)!} \quad (2.8)$$

*2.1.3 Simulated data.* The simulated images generated for use in testing the proposed algorithm will be 50-by-50 (high resolution) for the 2-D case and 13-by-13 (low resolution) for the 3-D case. These resolutions produce an undersampling factor of approximately four ( $L \approx 4$ ). The undersampling factor and resolutions were chosen because currently 2-D LADAR systems can easily achieve a pixel pitch of 25 micrometers while 3-D LADAR systems possess a 100 micrometer pixel pitch which produces an undersampling factor of four. The simulated 3-D data contains 20 simulated pulse returns.

The first target used to produce the simulated data is shown in figure 2(a). The figure depicts a two building target that is imaged onto a 50-by-50 target plane. The top of the buildings are located at 10000 meters and the ground is located at 10002 meters. The raw under sampled 3-D data produced an estimated range shown in figure 2(b). The estimated range is the result of using a cross-correlation range estimator (matched filter) which will be discussed in detail in section 3.2.

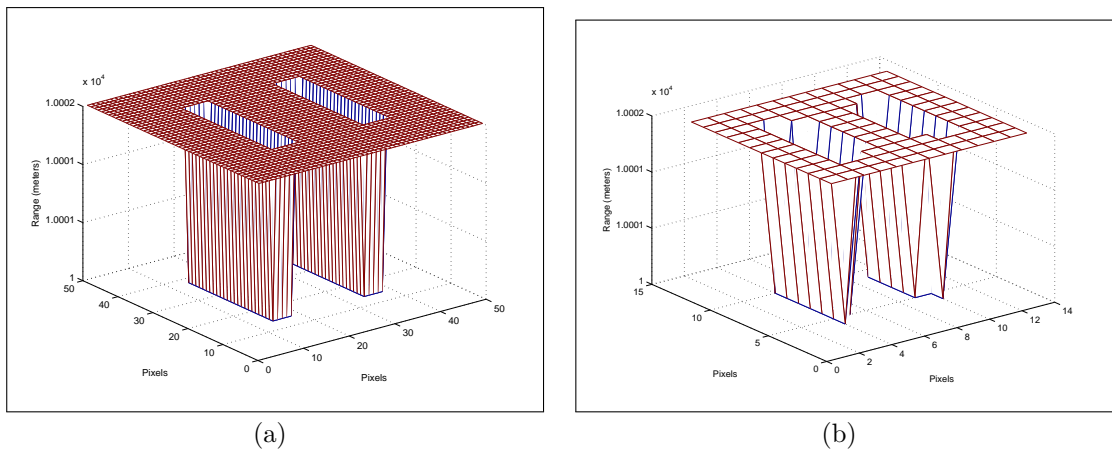


Figure 2.2: (a) The 50-by-50 target area. (b) The 13-by-13 raw estimated range from the undersampled 3-D data on the low resolution grid.

The 3-D data can also be represented by its 2-D images at each time instance. A time instance is governed by the pulse width of the laser. For the simulated systems the pulse width is two nanoseconds. The pulse width dictates the time it takes the pulse to hit the target and return back to the receiver. Figure 2.3 shows the 2-D images of the data cube for every other time instance. The images represent the image received by the LADAR system every four nanoseconds.

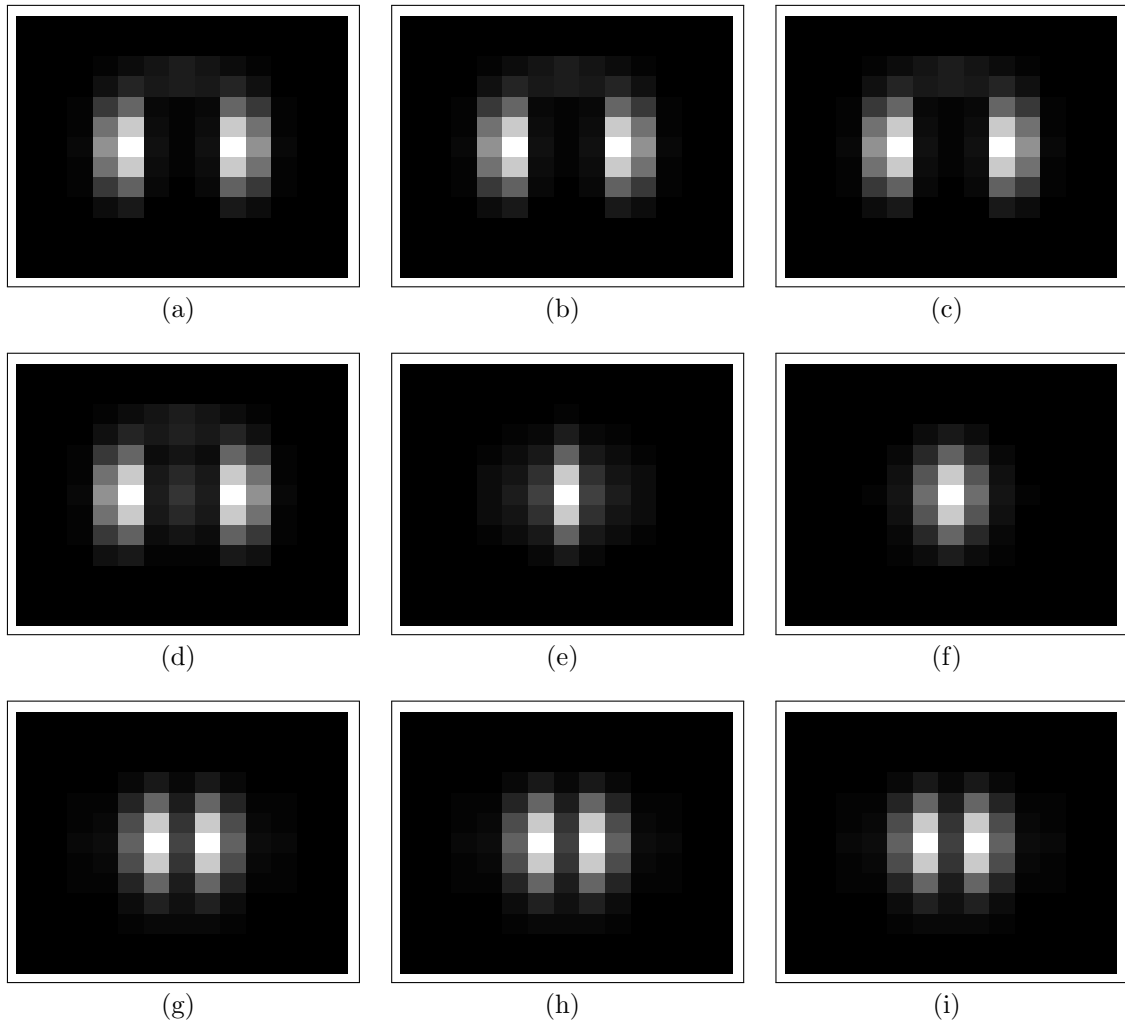


Figure 2.3: 2-D intensity images of the 3-D data cube over the course of 36 nanoseconds. Each image is shown on a 13-by-13 pixel grid and represents the data slice taken every 4 nanoseconds.

An enlarged image at the second time instance is shown in figure 2.4, the figure includes both high and low resolution images. The low resolution image is what a 3-D



LADAR system provides in 2-D. The sampling in this example makes it difficult to discern the actual structure of the object. The 3-D data is 13-by-13 and is pictorially different from the original target area. This provides the motivation for trying to improve the 3-D data through various methods. Figure 2.3(c) shows the 2-D image intensity which represents what a 2-D camera would see. The image was created by summing the high resolution images in the high resolution 3-D data cube.

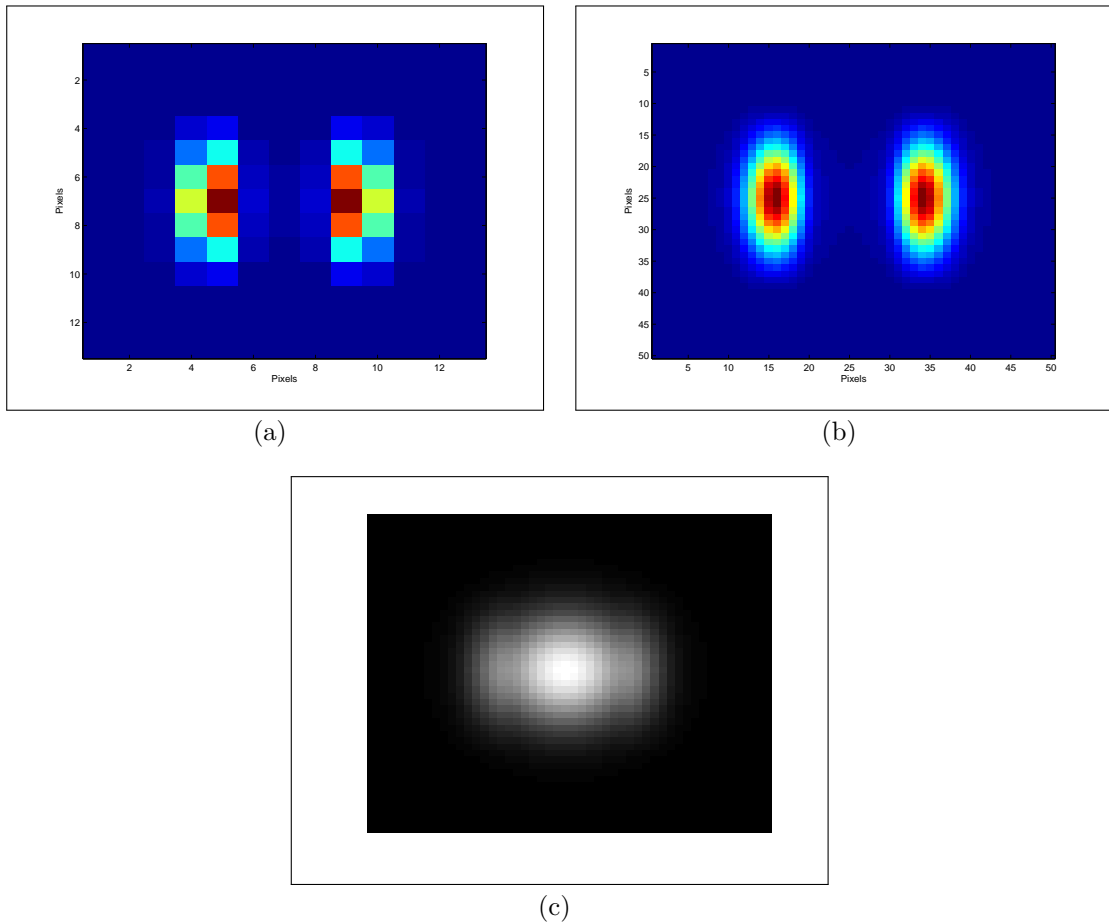


Figure 2.4: (a) The low resolution (13-by-13) data slice. (b) The high resolution (50-by-50) data slice. (c) The 2-D data to be fused with the 3-D data.

The second target used to produce the simulated data is more complicated. The target contains numerous buildings at different heights while the ground is still located 10002 meters from the LADAR system. The second target's profile is shown in figure 2.5.

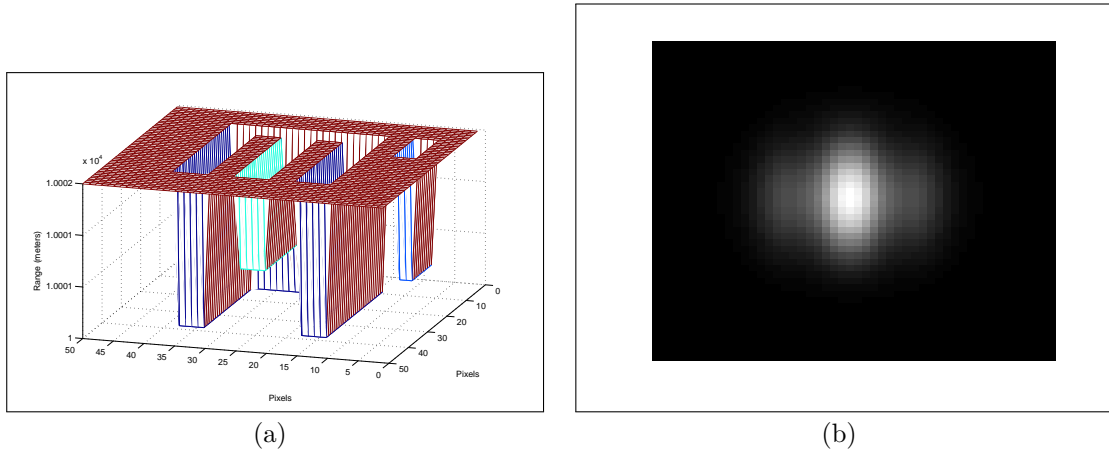


Figure 2.5: (a) 50-by-50 target area of the second simulation. (b) The 2-D image resulting from summing the second targets high resolution 3-D data cube.

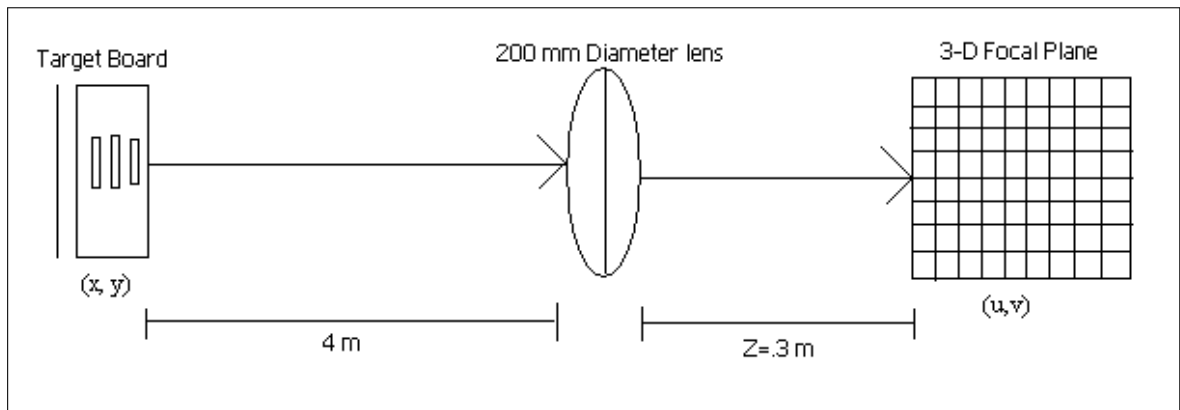


Figure 2.6: Setup to obtain measured data.

*2.1.4 Measured data.* The measured data was obtained from a 3-D LADAR system that shot a scene of a 3 bar cut out (third target) as depicted in figure 2.6. The system used 17 time samples to build a 3-D data cube. The system possesses a 128-by-128 grid of detectors. The system created 20 separate 3-D data cubes. Each image in the cube was cropped down to 64-by-64 in order to focus on the target area.

Unlike the simulated data, the measured data exhibits non-ideal behavior which includes but is not limited to gain variation and electronic noise. When the LADAR system shoots a scene a gain drop exists due to the laser being incident on a larger area in the detector array [11]. This phenomena causes a gain variation between

the first and second surfaces. The LADAR system used to create the data is not a photon counting system. In photon counting systems every detected return equals one photon. The proposed algorithm does not take into account gain variation or photon counting conversion factors in order to simplify the algorithm's development. [11] shows how to correct for this behavior. The data used is raw data that contain these effects in it without correction.

Another parameter is needed to use the measured data and it is the system's optical cutoff frequency,  $f_c$ . The cutoff frequency of the system is determined by using Eq. (2.9) [4]. The diameter ( $D$ ) and focal distance ( $Z$ ) are shown in figure 2.6 and the wavelength ( $\lambda$ ) of the system is 1.55 micrometers. In order to achieve the correct sampling rate the Nyquist rate must be used which is two times the cutoff frequency. This makes the sampling rate 116.25 micrometers [10]. Since The pixel pitch is 100 micrometers, the 3-D cube from the data is oversampled.

$$f_c = \frac{D}{\lambda Z} \quad (2.9)$$

Since the measured data is critically sampled the true range can be extracted from it. The true range is created from averaging all the ranges from each data cube and subtracting the mean of the analyzed cube. The fifth data cube was used for this research. The measured data range information is in terms of pulse returns (samples). The true range for the measured data is shown in figure 2.7.

Downsampling the measured data creates under sampled data that will be used for analysis in this research. This downsampling effect captures the effect of a larger pixel and data aliasing. The effect of downsampling an image in the cube is shown in figure 2.8.

The downsampling effect shown in figure 2.6(a) is also seen in all the images of the measured data cube. The images produced by every other pulse return are shown in figure 2.9.

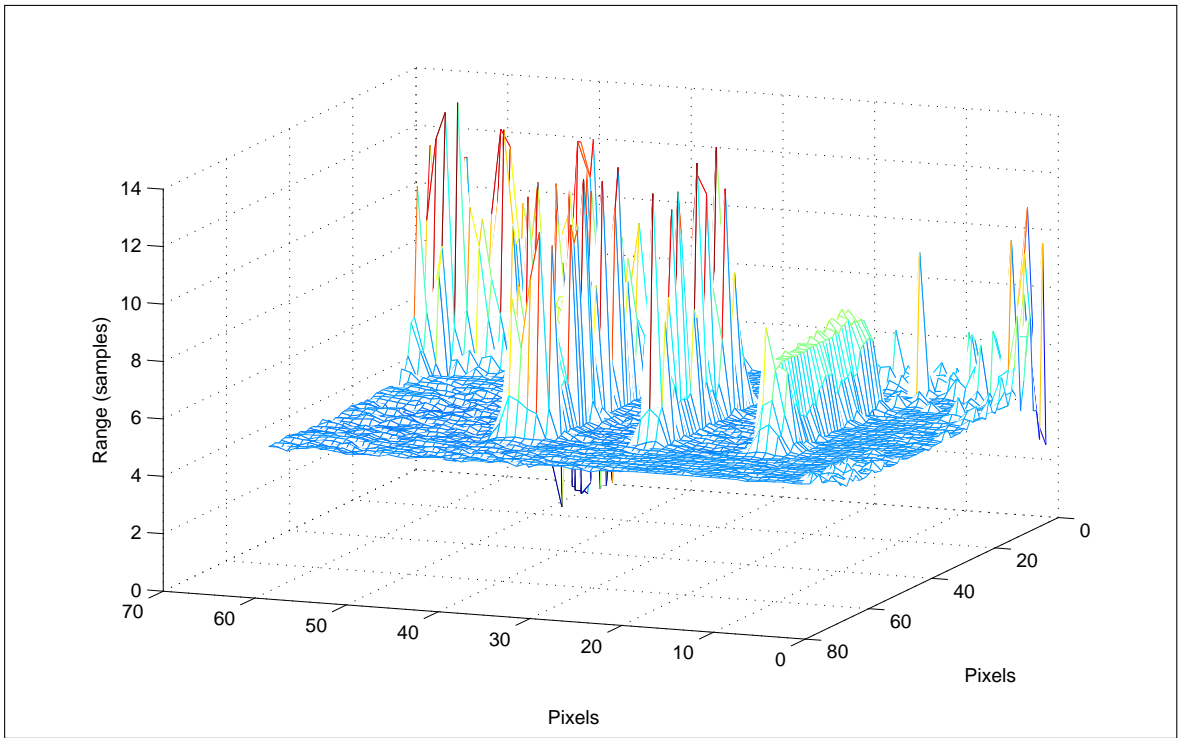


Figure 2.7: Target area of measured data on a 64-by-64 grid.

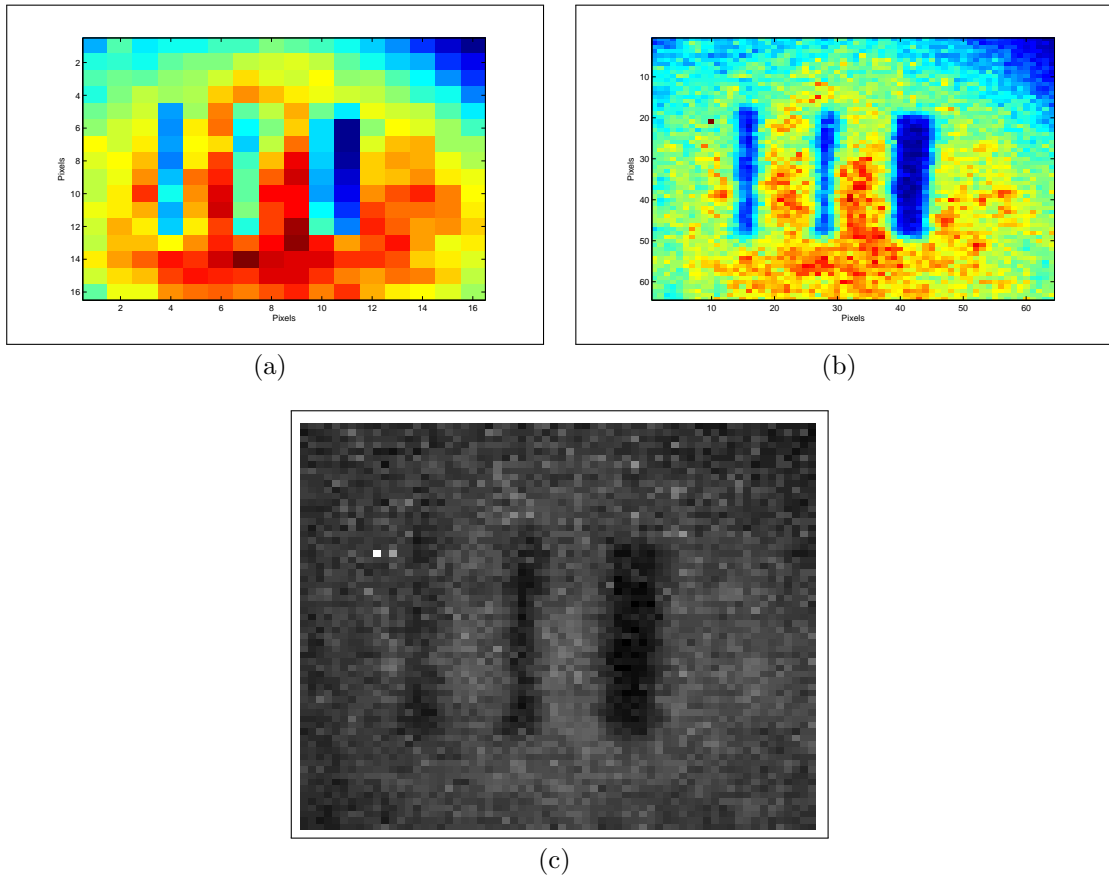


Figure 2.8: (a) The low resolution (16-by-16) data slice. (b) The high resolution (64-by-64) data slice. (c) The 2-D data that will be fused with the 3-D data.

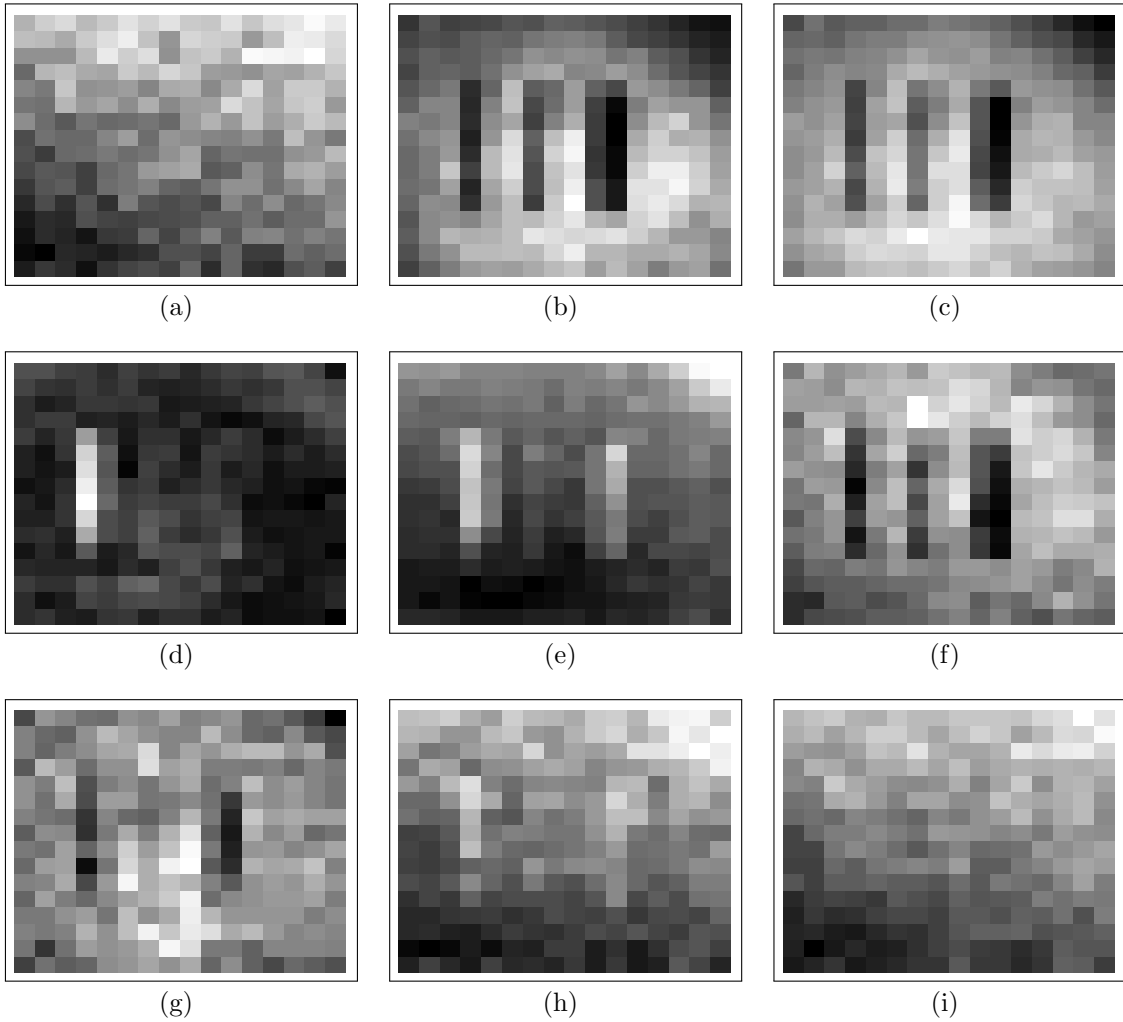


Figure 2.9: 2-D intensity images of the 3-D measured data cube. Each image is shown on a 16-by-16 pixel grid.

### III. Research Methodology

This chapter describes the methods used to derive the proposed sensor fusion algorithm as well as interpolation methods used for comparison. The first section will describe the use of the EM algorithm to estimate both the range and bias of the LADAR signals. The second section will detail the types of interpolation that will be used for comparison to the proposed algorithm. Using the equations in simulations and the results of those simulations will be the subject of chapter 4.

#### 3.1 Proposed Sensor Fusion Algorithm

The proposed algorithm is derived using an EM approach to estimate the range  $r(x, y)$  to each pixel in the target area and bias  $B(u, v)$  for each detector in the array. The proposed sensor fusion approach will estimate  $A(x, y)$  by using a Richardson-Lucy deconvolution [9] of the properly sampled 2-D data as shown in Eq. (3.1). This technique is an iterative process in which each iteration produces an  $A_{new}(x, y)$ .  $A_{old}(x, y)$  represents the estimate for  $A(x, y)$ ,  $d_{2d}(u, v)$  is the observed 2-D data, and  $i(u, v)$  is the estimated focal plane intensity.  $h(x, y)$  represents the total optical point spread function (PSF). For this work, it is assumed that the PSF is known. The initial estimate for  $A(x, y)$  is a constant.

$$A(x, y)_{new} = A(x, y)_{old} \sum_{v=1}^N \sum_{u=1}^N \frac{d_{2d}(u, v)}{i(u, v)} h(u - x, v - y) \quad (3.1)$$

The GEM approach proposed by McMahan [7] is similar to the EM approach in this work. They are not the equivalent because McMahan's work does not deal with undersampled data and does not feature the use of 2-D and 3-D data. The first step of the EM approach is to create a statistical model for the measured data, which is known as the incomplete data. Inventing a set of mythical data (complete data) and its relationship to the incomplete data is the second step. The third step is to select a statistical model for the complete data such that it adheres to the relationship of the complete to incomplete data. Next is to form a complete data log-likelihood.

In step five, the conditional expectation of the complete log-likelihood is computed with respect to the incomplete data. The last step is to maximize the conditional expectation with respect to the parameter that is being estimated. The following subsections describe the EM approach to estimate the range [3].

*3.1.1 Formulating complete and incomplete data.* As stated in chapter 2, the 3-D LADAR data (incomplete data) is a realization of a Poisson random variable at each pixel. The joint probability of the incomplete data is shown in Eq. (2.8). Due to the bias estimation the complete data will contain two variables,  $\tilde{d}_1(u, v, x, y, r_k)$  and  $\tilde{d}_2(u, v, r_k)$ . The incomplete data,  $d$ , has a relationship to the complete data as shown in Eq. (3.2).

$$d(u, v, r_k) = \sum_{x=1}^M \sum_{y=1}^M \tilde{d}_1(u, v, x, y, r_k) + \tilde{d}_2(u, v, r_k) \quad (3.2)$$

The variables  $(x, y)$  represent the target plane pixel locations and  $(u, v)$  represents the focal plane coordinates. The variable  $r_k$  represents discrete ranges each time the pulse is sampled by the 3-D system. The expectations (means) of the complete data are shown in Eq. (3.3). The means were chosen based on the complete data's relationship to the incomplete data.

$$\begin{aligned} E[\tilde{d}_1(u, v, x, y, r_k)] &= \frac{A(x, y)}{\sqrt{2\pi\sigma}} e^{\frac{(r_k - r(x, y))^2}{2\sigma^2}} h(Lu - x, Lv - y) \\ E[\tilde{d}_2(u, v, r_k)] &= B(u, v) \end{aligned}$$

Since the sum of two Poisson random variables is Poisson, the complete data can be modeled as a Poisson random variable at each pixel, retaining the validity of Eq. (3.3). Based on the chosen means, the complete data probabilities  $p_1$  and  $p_2$  are shown in Eq. (3.3).



$$\begin{aligned}
p_1[\tilde{d}_1(u, v, x, y, r_k)] &= \\
&\frac{\frac{A(x,y)}{\sqrt{2\pi\sigma}} e^{\frac{(r_k-r(x,y))^2}{2\sigma^2}} h(Lu-x, Lv-y) \tilde{d}_1(u,v,x,y,r_k) e^{-\frac{A(x,y)}{\sqrt{2\pi\sigma}} e^{\frac{(r_k-r(x,y))^2}{2\sigma^2}} h(Lu-x, Lv-y)}}{\tilde{d}_1(u, v, x, y, r_k)!} \\
p_2[\tilde{d}_2(u, v, r_k)] &= \\
&\frac{B(u, v) \tilde{d}_2(u,v,r_k) e^{-B(u,v)}}{\tilde{d}_2(u, v, r_k)!} \tag{3.3}
\end{aligned}$$

Taking the product of the probabilities at each sample location  $(x, y, u, v)$  and each range  $(r_k)$  produces the joint probability ( $p_3$ ) for the complete data, Eq. (3.4).

$$p_3 = \left[ \prod_{u=1}^M \prod_{v=1}^M \prod_{k=1}^K \prod_{x=1}^M \prod_{y=1}^M p_1[\tilde{d}_1(u, v, x, y, r_k)] \right] \times \left[ \prod_{u=1}^M \prod_{v=1}^M \prod_{k=1}^K p_2[\tilde{d}_2(u, v, r_k)] \right] \tag{3.4}$$

Taking the natural log of Eq. (3.4) produces the complete data log-likelihood shown in Eq. (3.5).

$$\begin{aligned}
L = \sum_{x=1}^M \sum_{y=1}^M \sum_{u=1}^M \sum_{v=1}^M \sum_{k=1}^K & [\tilde{d}_1(u, v, x, y, r_k) \ln\left(\frac{A(x, y)}{\sqrt{2\pi\sigma}} e^{\frac{(r_k-r(x,y))^2}{2\sigma^2}} h(Lu-x, Lv-y)\right) \\
& - \frac{A(x, y)}{\sqrt{2\pi\sigma}} e^{\frac{(r_k-r(x,y))^2}{2\sigma^2}} h(Lu-x, Lv-y) - \ln(\tilde{d}_1(u, v, x, y, r_k)!)] \\
& + \sum_{u=1}^M \sum_{v=1}^M \sum_{k=1}^K [\tilde{d}_2(u, v, r_k) \ln(B(u, v)) - B(u, v) - \ln(\tilde{d}_2(u, v, r_k)!)] \tag{3.5}
\end{aligned}$$

*3.1.2 Finding the expectation.* The conditional expectation of the complete data log-likelihood is found by taking the expectation with respect to the incomplete data, the pulse estimate ( $P_{old}(x, y, r_k)$ ), and the bias estimate ( $B_{old}(u, v)$ ). The

conditional expectation ( $Q$ ) in general form is shown in Eq. (3.6).

$$\begin{aligned}
Q = & \sum_{x=1}^M \sum_{y=1}^M \sum_{u=1}^M \sum_{v=1}^M \sum_{k=1}^K [E[\tilde{d}_1(u, v, x, y, r_k) | d(u, v, r_k), P_{old}(x, y, r_k), B_{old}(u, v)]] \\
& \times (\ln(\frac{A(x, y)}{\sqrt{2\pi}\sigma} h(Lu - x, Lv - y)) + \ln(e^{\frac{(r_k - r(x, y))^2}{2\sigma^2}})) - P(x, y, r_k) h(Lu - x, Lv - y) \\
& - E[\ln(\tilde{d}_1(u, v, x, y, r_k)!) | d(u, v, r_k), P_{old}(x, y, r_k), B_{old}(u, v)]] \\
& + \sum_{u=1}^M \sum_{v=1}^M \sum_{k=1}^K [E[(\tilde{d}_2(u, v, r_k) | d(u, v, r_k), P_{old}(x, y, r_k), B_{old}(u, v))] \ln(B(u, v))] \\
& - B(u, v) - E[(\tilde{d}_2(u, v, r_k)!) | d(u, v, r_k), P_{old}(x, y, r_k), B_{old}(u, v)]] \tag{3.6}
\end{aligned}$$

The variable  $I_{old}$  is the image produced from the pulse estimate, Eq. (3.7), which is needed to find each of the individual conditional expectations.

$$I_{old}(u, v, r_k) = \sum_{x=1}^N \sum_{y=1}^N P_{old}(x, y, r_k) h(Lu - x, Lv - y) + B_{old}(u, v) \tag{3.7}$$

The solution for the individual conditional expectations are shown in Eq. (3.8) [12].

$$\begin{aligned}
E[\tilde{d}_1(u, v, x, y, r_k) | d(u, v, r_k), P_{old}(x, y, r_k), B_{old}(u, v)] = & \frac{d(u, v, r_k) P_{old}(x, y, r_k) h(Lu - x, Lv - y)}{I_{old}(u, v, r_k)} \\
E[\tilde{d}_2(u, v, r_k) | d(u, v, r_k), P_{old}(x, y, r_k), B_{old}(u, v)] = & \frac{d(u, v, r_k) B_{old}(u, v)}{I_{old}(u, v, r_k)} \tag{3.8}
\end{aligned}$$

Substituting the previous result back into  $Q$  produces Eq. (3.9).

$$\begin{aligned}
Q = & \sum_{x=1}^M \sum_{y=1}^M \sum_{u=1}^M \sum_{v=1}^M \sum_{k=1}^K \left[ \frac{d(u, v, r_k) P_{old}(x, y, r_k) h(Lu - x, Lv - y)}{I_{old}(u, v, r_k)} \right. \\
& \times \left( \ln \left( \frac{A(x, y)}{\sqrt{2\pi}\sigma} h(Lu - x, Lv - y) \right) - \frac{(r_k - r(x, y))^2}{2\sigma^2} \right) \\
& - \frac{A(x, y)}{\sqrt{2\pi}\sigma} e^{\frac{(r_k - r(x, y))^2}{2\sigma^2}} h(Lu - x, Lv - y) \\
& - E[\ln(\tilde{d}_1(u, v, x, y, r_k)) | d(u, v, r_k), P_{old}(x, y, r_k), B_{old}(u, v)]] \\
& + \sum_{u=1}^M \sum_{v=1}^M \sum_{k=1}^K \left[ \frac{d(u, v, r_k) B_{old}(u, v)}{I_{old}(u, v, r_k)} \ln(B(u, v)) \right. \\
& \left. - B(u, v) - E[(\tilde{d}_2(u, v, r_k)) | d(u, v, r_k), P_{old}(x, y, r_k), B_{old}(u, v)]] \right] \quad (3.9)
\end{aligned}$$

*3.1.3 Maximizing the Expectation.* With the conditional expectation found the next step is to maximize it with respect to the range and the bias. Taking the derivative of  $Q$  with respect to  $r(x_0, y_0)$ , then setting the derivative equal to zero and solving for  $r(x, y)$  will maximize the conditional expectation for the range at each point in the scene. Doing the same with respect to the bias will maximize the conditional expectation for the bias. The bias and range will be estimated separately. In order to estimate the range an assumption is made that the pulse always exists in the range gate. This removes all range dependence from the sum of  $I(u, v, r_k)$  as shown in Eq. (3.10). The variable  $C$  represents a constant.

$$\sum_{x=1}^M \sum_{y=1}^M \sum_{u=1}^M \sum_{v=1}^M \sum_{k=1}^K \frac{A(x, y)}{\sqrt{2\pi}\sigma} e^{\frac{(r_k - r(x, y))^2}{2\sigma^2}} h(Lu - x, Lv - y) = C \quad (3.10)$$

Since the bias portion (second summation group of Eq. (3.9)) of  $Q$  does not depend on  $r(x, y)$ , its derivative with respect to the range goes to zero. Given this

property and Eq. (3.10),  $Q$  reduces to Eq. (3.11).

$$\begin{aligned}
Q = & \sum_{x=1}^M \sum_{y=1}^M \sum_{u=1}^M \sum_{v=1}^M \sum_{k=1}^K \left[ \frac{d(u, v, r_k) P_{old}(x, y, r_k) h(Lu - x, Lv - y)}{I_{old}(u, v, r_k)} \right. \\
& \times \left( \ln \left( \frac{A(x, y)}{\sqrt{2\pi}\sigma} h(Lu - x, Lv - y) \right) - \frac{(r_k - r(x, y))^2}{2\sigma^2} \right) \\
& \left. - C - E[\ln(\tilde{d}_1(u, v, x, y, r_k)! | d(u, v, r_k), P_{old}(x, y, r_k), B_{old}(u, v))] \right] + 0 \quad (3.11)
\end{aligned}$$

Taking the derivative of the first piece of Eq. (3.11) with respect to  $r(x_0, y_0)$  results in Eq. (3.12)

$$\begin{aligned}
& \frac{\partial}{\partial(r(x_0, y_0))} \left[ \frac{d(u, v, r_k) P_{old}(x, y, r_k) h(Lu - x, Lv - y)}{I_{old}(u, v, r_k)} \right. \\
& \times \left. \left( \ln \left( \frac{A(x, y)}{\sqrt{2\pi}\sigma} h(Lu - x, Lv - y) \right) - \frac{(r_k - r(x, y))^2}{2\sigma^2} \right) \right] = \\
& \frac{d(u, v, r_k) P_{old}(x, y, r_k) h(Lu - x, Lv - y)}{I_{old}(u, v, r_k)} \frac{\partial}{\partial(r(x_0, y_0))} \left( -\frac{(r_k - r(x, y))^2}{2\sigma^2} \right) = \\
& \frac{d(u, v, r_k) P_{old}(x, y, r_k) h(Lu - x, Lv - y)}{I_{old}(u, v, r_k)} \frac{(2r_k - 2r(x, y))}{2\sigma^2} \frac{\partial(r(x, y))}{\partial(r(x_0, y_0))} = \\
& \frac{d(u, v, r_k) P_{old}(x, y, r_k) h(Lu - x, Lv - y)}{I_{old}(u, v, r_k)} \frac{(r_k - r(x, y))}{\sigma^2} \delta(x - x_0, y - y_0) \quad (3.12)
\end{aligned}$$

The derivative of the second piece of Eq. (3.11) is shown to be zero in Eq. (3.13). This result is due to the conditional expectation of the complete data, given the incomplete data and old estimates, will not be a function of the new estimates thus rendering zero dependency on  $r(x, y)$ .

$$\frac{\partial}{\partial(r(x_0, y_0))} E[\ln(\tilde{d}_1(u, v, x, y, r_k)! | d(u, v, r_k), P_{old}(x, y, r_k), B_{old}(u, v))] = 0 \quad (3.13)$$

Using Eqs. (3.10), (3.12), and (3.13), the general form  $\frac{\partial Q}{\partial(r(x_0, y_0))}$  is shown in Eq. (3.14).

$$\begin{aligned} \frac{\partial Q}{\partial(r(x_0, y_0))} = & \sum_{x=1}^M \sum_{y=1}^M \sum_{u=1}^M \sum_{v=1}^M \sum_{k=1}^K \left[ \frac{d(u, v, r_k)}{I_{old}(u, v, r_k)} P_{old}(x, y, r_k) h(Lu - x, Lv - y) \right. \\ & \left. \times \frac{(r_k - r(x, y))}{\sigma^2} \delta(x - x_0, y - y_0) \right] \end{aligned} \quad (3.14)$$

Applying the sifting property to Eq. (3.14) removes the summations over  $x$  and  $y$  and results in the  $Q$  that will be maximized (Eq. (3.15)).

$$\frac{\partial Q}{\partial(r(x_0, y_0))} = \sum_{u=1}^M \sum_{v=1}^M \sum_{k=1}^K \frac{d(u, v, r_k)}{I_{old}(u, v, r_k)} P_{old}(x_0, y_0, r_k) h(Lu - x_0, Lv - y_0) \frac{(r_k - r(x_0, y_0))}{\sigma^2} \quad (3.15)$$

Setting Eq. (3.15) equal to zero results in Eq. (3.16).

$$0 = \sum_{u=1}^M \sum_{v=1}^M \sum_{k=1}^K \frac{d(u, v, r_k)}{I_{old}(u, v, r_k)} P_{old}(x_0, y_0, r_k) h(Lu - x_0, Lv - y_0) \frac{(r_k - r(x_0, y_0))}{\sigma^2} \quad (3.16)$$

Distributing  $r_k$  and  $r(x_0, y_0)$  makes Eq. (3.16) easier to manipulate (Eq. (3.17)).

$$\begin{aligned} 0 = & r(x_0, y_0) \sum_{u=1}^M \sum_{v=1}^M \sum_{k=1}^K \frac{d(u, v, r_k)}{I_{old}(u, v, r_k)} P_{old}(x_0, y_0, r_k) h(Lu - x_0, Lv - y_0) \\ & - \sum_{u=1}^M \sum_{v=1}^M \sum_{k=1}^K r_k \frac{d(u, v, r_k)}{I_{old}(u, v, r_k)} P_{old}(x_0, y_0, r_k) h(Lu - x_0, Lv - y_0) \end{aligned} \quad (3.17)$$

Moving the terms from one side to the other in Eq. (3.17), then separating the terms provides a solution, Eq. (3.18), that is iterative and updates  $r(x_0, y_0)$  for each

iteration.

$$r(x_0, y_0) = \frac{\sum_{k=1}^K r_k P_{old}(x_0, y_0, r_k) \sum_{u=1}^M \sum_{v=1}^M \frac{d(u, v, r_k)}{I_{old}(u, v, r_k)} h(Lu - x_0, Lv - y_0)}{\sum_{k=1}^K P_{old}(x_0, y_0, r_k) \sum_{u=1}^M \sum_{v=1}^M \frac{d(u, v, r_k)}{I_{old}(u, v, r_k)} h(Lu - x_0, Lv - y_0)} \quad (3.18)$$

The same process is used to solve for the bias. The range portion (first summation group of Eq. (3.9)) of  $Q$  does not contain the bias variable and does not depend on  $Q$ , its derivative with respect to  $B(u_0, v_0)$  is zero reducing  $Q$  to Eq. (3.19).

$$Q = \sum_{u=1}^M \sum_{v=1}^M \sum_{k=1}^K \left[ \frac{d(u, v, r_k) B_{old}(u, v)}{I_{old}(u, v, r_k)} \ln(B(u, v)) - B(u, v) - E[(\tilde{d}_2(u, v, r_k)! | d(u, v, r_k), P_{old}(x, y, r_k), B_{old}(u, v))] \right] \quad (3.19)$$

Taking the partial derivative the first piece of Eq. (3.19) with respect to the bias,  $B(u, v)$ , is shown in Eq. (3.20).

$$\begin{aligned} \frac{\partial}{\partial(B(u_0, v_0))} \frac{d(u, v, r_k) B_{old}(u, v)}{I_{old}(u, v, r_k)} \ln(B(u, v)) &= \\ \frac{d(u, v, r_k) B_{old}(u, v)}{I_{old}(u, v, r_k)} \frac{\partial}{\partial(B(u_0, v_0))} \ln(B(u, v)) &= \\ \frac{d(u, v, r_k) B_{old}(u, v)}{I_{old}(u, v, r_k) B(u, v)} \frac{\partial(B(u, v))}{\partial(B(u_0, v_0))} &= \\ \frac{B_{old}(u, v) d(u, v, r_k)}{I_{old}(u, v, r_k) B(u, v)} \delta(u - u_0, v - v_0) & \end{aligned} \quad (3.20)$$

The partial derivative of  $B(u, v)$ , second piece of Eq. (3.19), results in a Dirac delta.

$$\frac{\partial}{\partial(B(u_0, v_0))} B(u, v) = \delta(u - u_0, v - v_0) \quad (3.21)$$

The derivative of the last piece of Eq. (3.19) is shown to be zero in Eq. (3.22). This result is due to the conditional expectation not depending on new estimates.

$$\frac{\partial}{\partial(B(u_0, v_0))} E[\ln(\tilde{d}_2(u, v, r_k)!)|d(u, v, r_k), P_{old}(x, y, r_k), B_{old}(u, v)] = 0 \quad (3.22)$$

Using Eqs. (3.20), (3.21), and (3.22), the general form of the derivative of  $Q$  with respect to  $B(u_0, v_0)$  becomes Eq. (3.23).

$$\begin{aligned} \frac{\partial Q}{\partial(B(u_0, v_0))} = & \\ & \sum_{u=1}^M \sum_{v=1}^M \sum_{k=1}^K \delta(u - u_0, v - v_0) \left[ \frac{B_{old}(u, v)d(u, v, r_k)}{I_{old}(u, v, r_k)B(u, v)} - 1 \right] \end{aligned} \quad (3.23)$$

Applying the sifting property to Eq. (3.23) results in Eq. (3.24)

$$\frac{\partial Q}{\partial(B(u_0, v_0))} = \sum_{k=1}^K \frac{B_{old}(u_0, v_0)d(u, v, r_k)}{I_{old}(u, v, r_k)B(u_0, v_0)} - 1 \quad (3.24)$$

Setting Eq. (3.23) equal to zero and separating terms results in the direct solution for estimating the bias, Eq. (3.25). The solution is iterative and updates  $B(u_0, v_0)$  for each iteration. The solutions for both range and bias are iterative and must be solved concurrently to estimate each one properly.

$$B(u_0, v_0) = B_{old}(u_0, v_0) \frac{\sum_{k=1}^K \frac{d(u, v, r_k)}{I_{old}(u, v, r_k)}}{K} \quad (3.25)$$

From the equations described in this section, the algorithm begins by estimating properly sampled 2-D data. The algorithm then uses the 2-D and 3-D data to estimate both range and bias. The estimates are then used to create new estimates with each iteration. This provides for improved range and bias estimates every iteration, ultimately improving the range accuracy of the raw 3-D data.

### 3.2 Data Interpolation

Interpolation is a method in which new data points are created from a set of under sampled data points. Data interpolation can be done in numerous ways, for the purpose of this paper we will focus on the pixel replication (zero-order), linear (first-order), and cubic interpolators [8]. An interpolator takes the data given to it and creates new data to a desired range. In this paper, the interpolator will take a 13-by-13 image and create a 50-by-50 image. Interpolating the data is a relatively quick process and is a standalone method. These attributes make data interpolation an attractive method for extracting information from the 3-D LADAR system.

Each interpolator has a single basis equation, which is manipulated at each higher order. The basis equation is representative of what an interpolator performs on image  $i(n, m)$ , an  $N_1$ -by- $M_1$  under sampled image. Eq. (3.26) shows the basis equation for interpolating data. The first part of the equation is creating a comb of the image,  $i_{comb}$ , that is sampled at rate  $L$ .  $L$  is determined by the following equality,  $M_1L = M$ . For example, producing a 50-by-50 image from a 25-by-25 image would dictate  $L = 2$ . The comb spreads the under sampled image out to the desired resolution, placing zeros around each pixel. A sample comb and image pair is shown in figure 3.1. Figure 1(b) shows how the comb spreads the under sampled image out to the desired resolution, placing zeros around each pixel. Convoluting the comb with a filter,  $g(n, m)$ , produces the interpolated image. The filter type dictates the type of interpolator being used.

$$\begin{aligned}
 i_{comb}(n_2, m_2) &= \sum_{n=1}^{N_1} \sum_{m=1}^{M_1} i(n, m) \delta(Ln - n_2) \delta(Lm - m_2) \\
 i_{int}(n, m) &= \sum_{n_2=1}^N \sum_{m_2=1}^M i_{comb}(n_2, m_2) g(n - n_2, m - m_2)
 \end{aligned} \tag{3.26}$$

For the case of the pixel replication interpolator the filter used is a rect that is  $L$ -by- $L$ . This means that the pixel replication interpolator takes the closest pixels



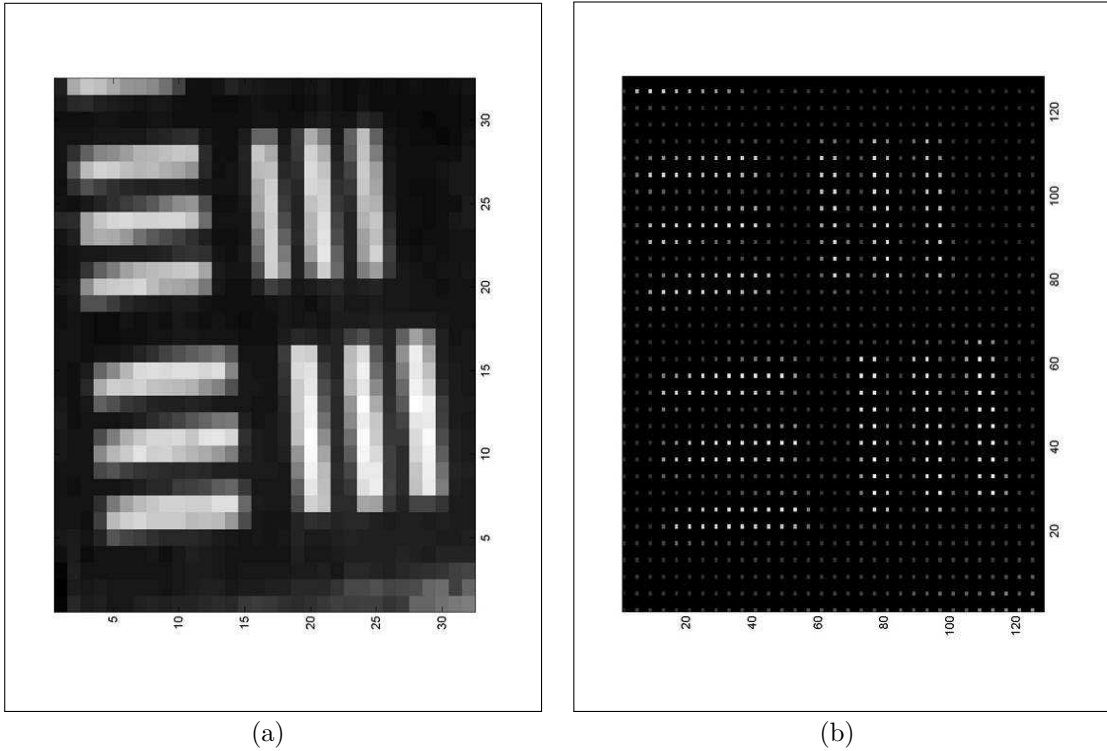


Figure 3.1: (a) 32-by-32 sample image. (b) Comb of the sample image on a 128 pixel grid.

and replicates them out to  $L$  pixels around that pixel. The linear interpolator uses a triangle filter that is created by convoluting two  $L$ -by- $L$  rect filters. This allows for the use of another pixel's information in the area of the interpolated pixel, rather than just replicating it. Finally, the cubic interpolator uses a piecewise function as its filter. Eq. (3.27) shows the piecewise function in the x-dimension. The coefficient  $a$  is calculated based on the interpolation size,  $N$ -by- $M$ .

$$g(x) = \begin{cases} (a+2)|x|^3 - (a+3)|x|^2 + 1, & 0 \leq |x| < 1 \\ a|x|^3 - 5a|x|^2 + 4a, & 1 \leq |x| < 2 \\ 0, & 2 \leq |x| \end{cases} \quad (3.27)$$

The interpolators only rely on the 3-D LADAR data and they do not take into account the 2-D LADAR data. Interpolation is not complete itself without a way

to estimate the range. This research will apply a cross-correlation range estimator (matched filter) to all the interpolated images. The matched filter uses a cross correlation function shown in Eq. (3.28) [10] and assumes a target is detected. The  $C(R)$  represents the correlation of the range,  $D_k$  is the data,  $P_t[k - 2R/(c\Delta t)]$  is the wave form. The value  $R$  represents a single range in a set of ranges. The range set determines how fine the range estimates become. The function produces a value for each range in the set, the range affiliated with the maximum value is the range chosen.

$$C(R) = \sum_{k=1}^{N_s} D_k P_t[k - 2R/(c\Delta t)] \quad (3.28)$$

## IV. Results and Analysis

This chapter presents the results of applying the methods described in Chapter 3 to the data described in Chapter 2. Section 4.1 details the results found when all four methods are applied to the simulated data. Section 4.2 discusses the results of the methods applied to the measured data. The *root mean square error* (RMSE) and graphs of the range will represent the results from each method. This analysis will calculate the RMSE between the target area (true range) and estimated ranges as shown Eq. (4.1).  $Range_{est}$  is the estimated range of the reconstruction method and  $Range_{truth}$  is the target area described in Chapter 2. The variable  $M$  represents the number of pixels in each dimension on the high resolution grid.

$$RMSE = \sqrt{\frac{\sum_{x=1}^M \sum_{y=1}^M (Range_{est}(x, y) - Range_{truth}(x, y))^2}{M^2}} \quad (4.1)$$

### 4.1 Simulated target results

The first target discussed in Chapter 2 was put through 400 iterations of the proposed algorithm, starting at a flat range. After 400 iterations, the algorithm achieved a root mean square error of approximately 222 millimeters. Figure 4.1 demonstrates how fast the update moved to the achieved range RMSE. The number of iterations where chosen based on the graph shown in figure 4.1, the full convergence of the algorithm happens at approximately iteration 325.

After estimating the range of the first target with the proposed algorithm, the Pixel Replication interpolator was used on the data. The Pixel Replication interpolator takes the data and spreads it out from 13-by-13 grid of pixels to 50-by-50 grid. This interpolator achieved a range RMSE of 333 millimeters. Then the linear interpolator was applied to the data as well. The linear interpolator achieved a range RMSE of 427 millimeters. The cubic interpolator achieved a range RMSE of 420 millimeters. The estimated ranges produced by the interpolators and proposed algorithm are shown in figure 4.2. Figure 4.2 shows the range portrayed on to a 3-D grid. Table

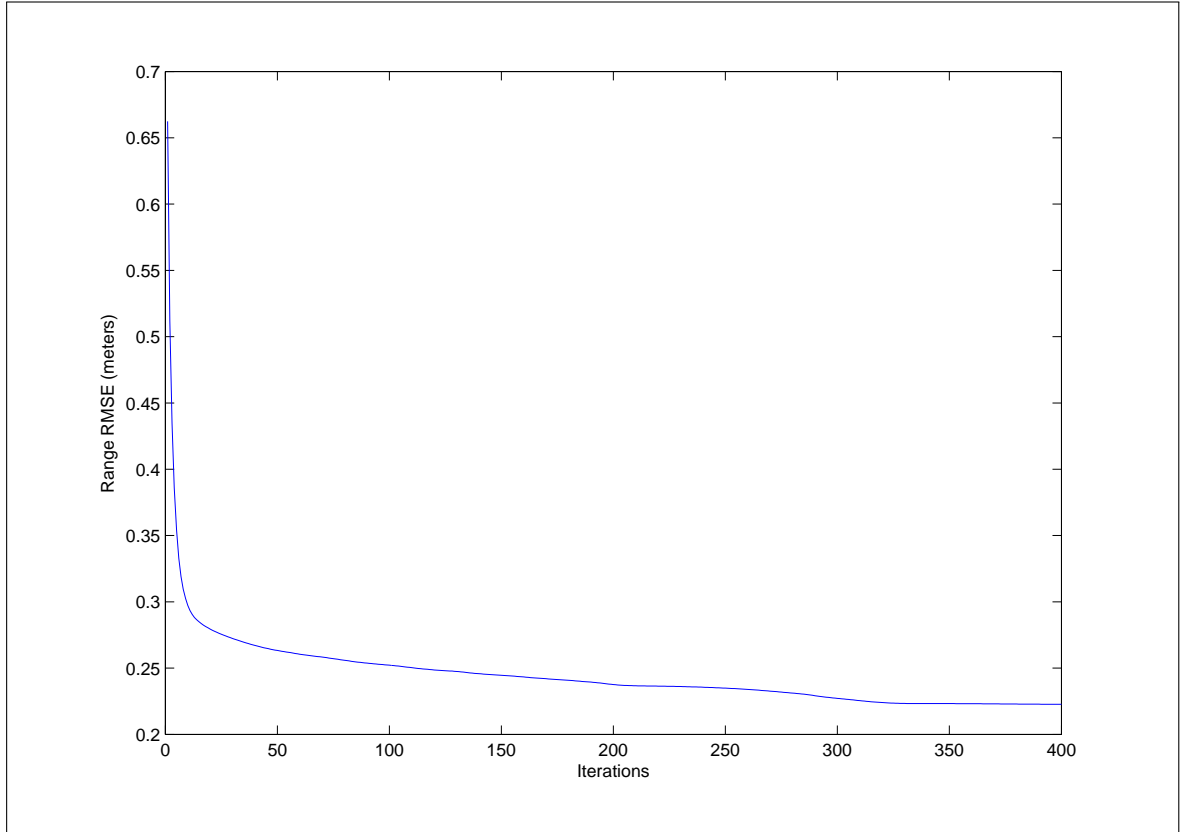


Figure 4.1: Range RMSE vs iterations after applying the proposed algorithm to the first target. This graph shows the RMSE reducing drastically between zero and fifty iterations. Due to the steady tail of the data, more than 400 iterations of the algorithm would only make minor reductions in RMSE of the range.

4.1 shows the comparison of all methods of improving range estimation for the first target.

The proposed algorithm then used to estimate the range to the second target starting from a flat range. Due to the beam shape the error was taken within a 36-by-28 box starting from pixel location (10, 14). The number of iterations completed by the proposed algorithm was 800 and resulted in a RMSE of 132 millimeters. Figure 4.3 shows the RMSE as a function of iteration count.

Interpolators were then used to estimate the range of the second target. The pixel replication interpolator achieved a range RMSE of 417 millimeters. The linear interpolator achieved a range RMSE of 451 millimeters. The cubic interpolator

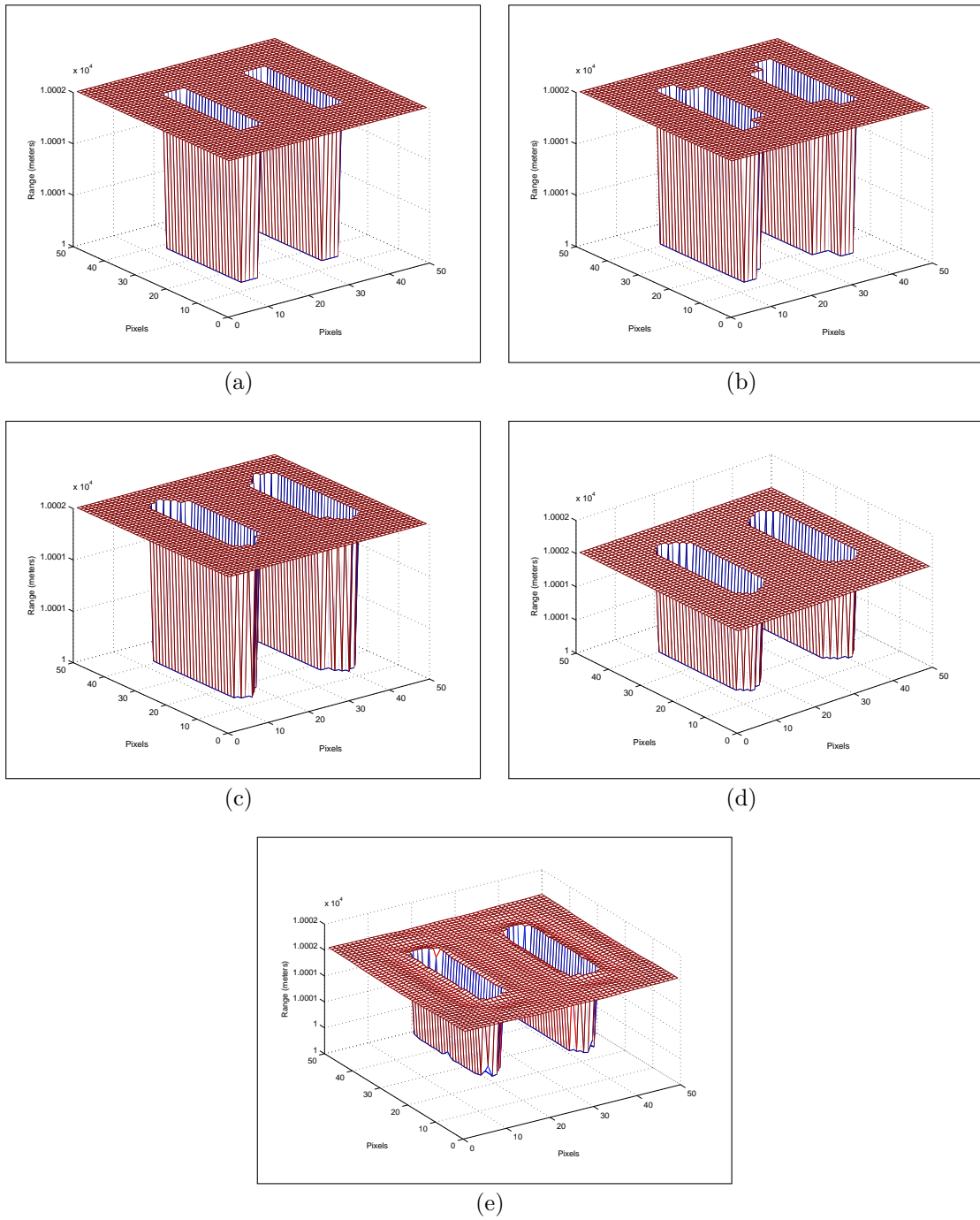


Figure 4.2: (a) 50-by-50 range truth of the first target. First target 50-by-50 estimated ranges: (b) Pixel replication estimated range. (c) Linear estimated range. (d) Cubic estimated range. (e) EM algorithm's estimated range.

Table 4.1: Method comparison for the first target

Method	Range RMSE
Proposed Algorithm	222 mm
Pixel Replication	333 mm
Linear Interpolation	427 mm
Cubic Interpolation	420 mm

achieved a range RMSE of 445 millimeters. Due to the high error of each interpolator's estimated range, the visual result of the range estimates will be shown on a 50-by-50 2-D range map and are shown in figure 4.4. The color bar in each subfigure represents range in meters. Table 4.2 shows the comparison of all methods of improving range estimation for the second target.

Table 4.2: Method comparison for the second target

Method	Range RMSE
Proposed Algorithm	132 mm
Pixel Replication	417 mm
Linear Interpolation	451 mm
Cubic Interpolation	445 mm

## 4.2 Measured data results

The final results of this research were obtained by applying the methods discussed in Chapter 3 to the downsampled (16-by-16) measured data described in Chapter 2. The results of the methods will be shown and compared on a 40-by-40 grid in order to diminish the edge noise seen in figure 2.7. The algorithm ran for 130 iterations and resulted in a range RMSE of 721 millimeters. The RMSE versus iteration number is shown in figure 4.5.

The interpolators were then applied to the downsampled measured data. The pixel replication interpolator achieved a range RMSE of 779 millimeters. The linear interpolator resulted in a range RMSE of 787 millimeters. The cubic interpolator achieved a range RMSE of 788 millimeters. The estimated range graphs of the inter-

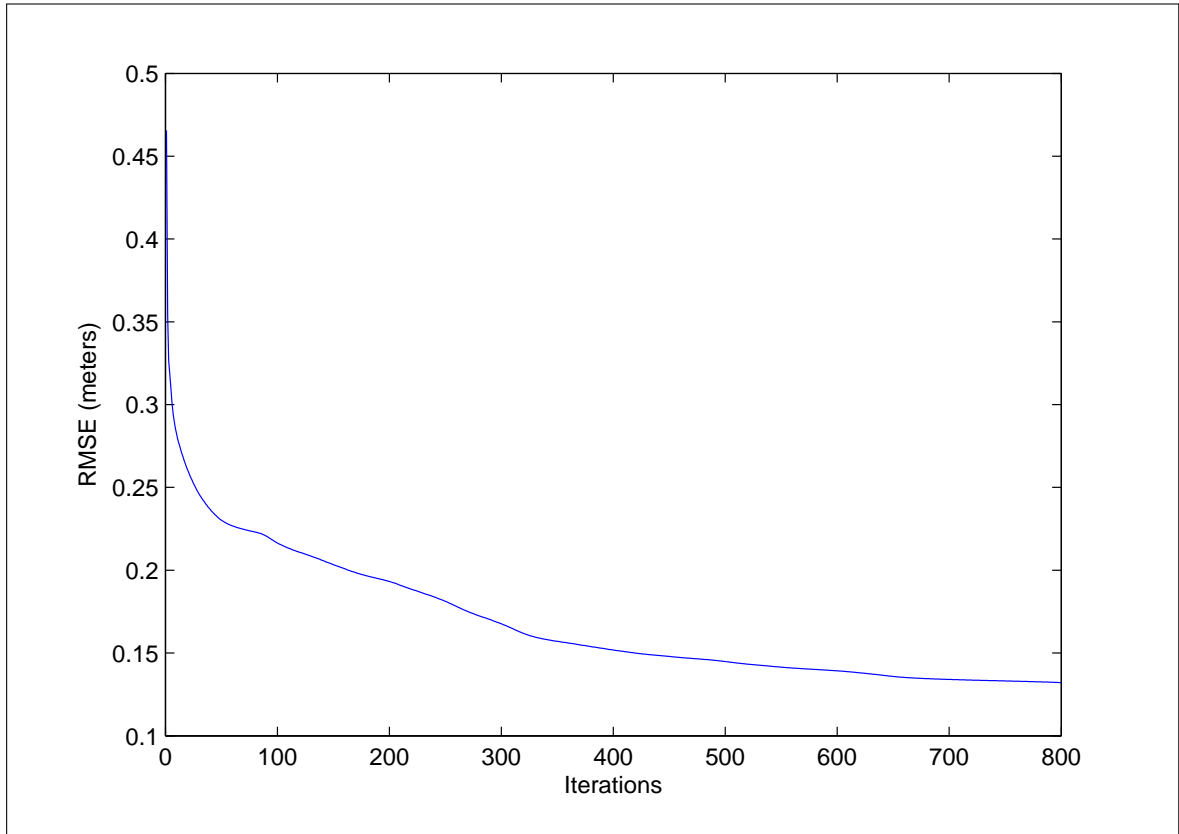


Figure 4.3: Range RMSE vs iterations after applying the proposed algorithm to the second target. This graph shows a great reduction in RMSE happening between zero and approximately seventy-five. The algorithm reached approximate convergence at a slower rate for this target as compared to the first target.

polators and proposed algorithm are shown in figure 4.6. The comparison of all the methods applied to the measured data is shown in table 4.3.

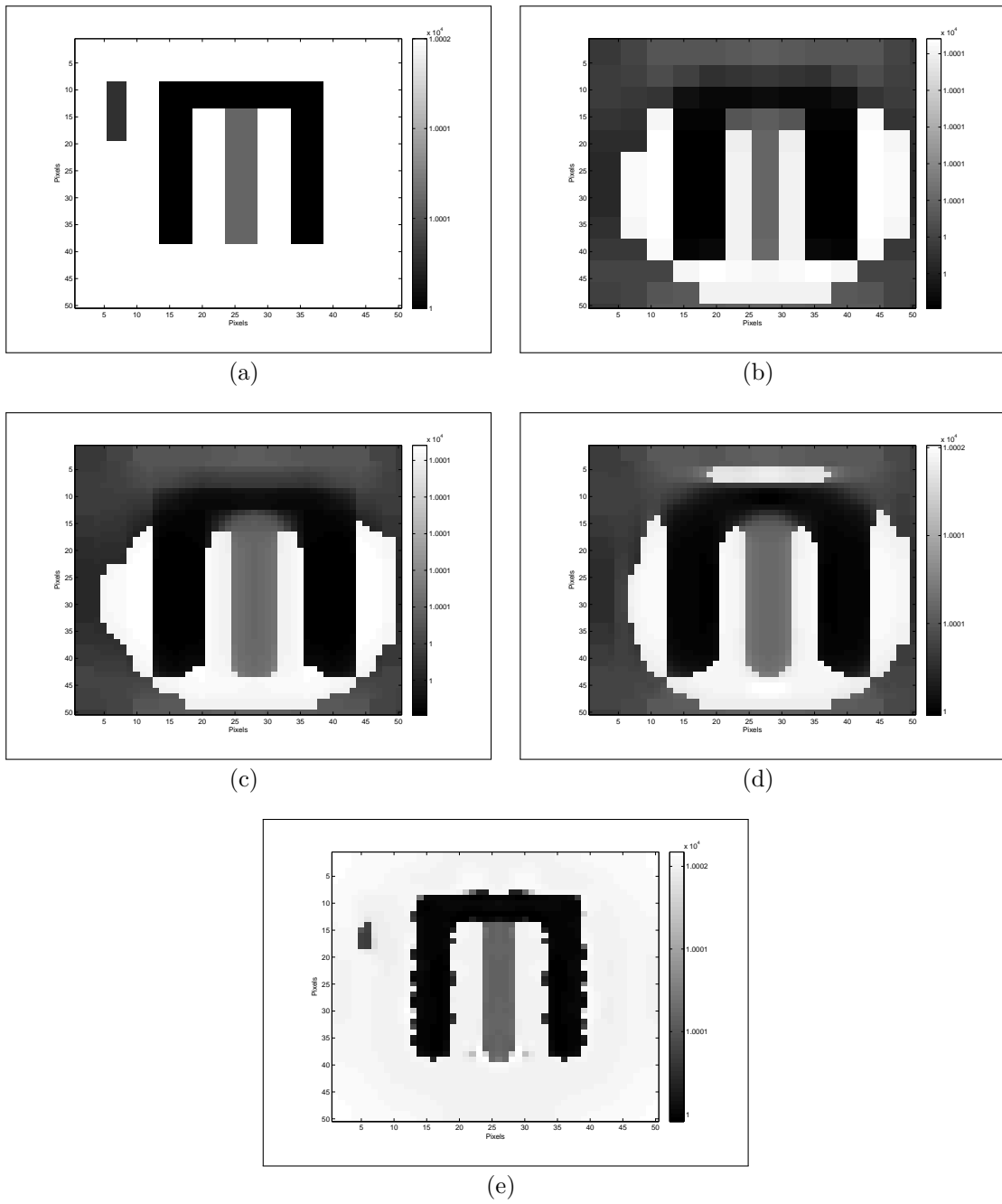


Figure 4.4: (a) 50-by-50 2-D range truth of the second target. Second target 50-by-50 2-D estimated ranges: (b) Pixel replication estimated range. (c) Linear estimated range. (d) Cubic estimated range. (e) EM algorithm's estimated range.



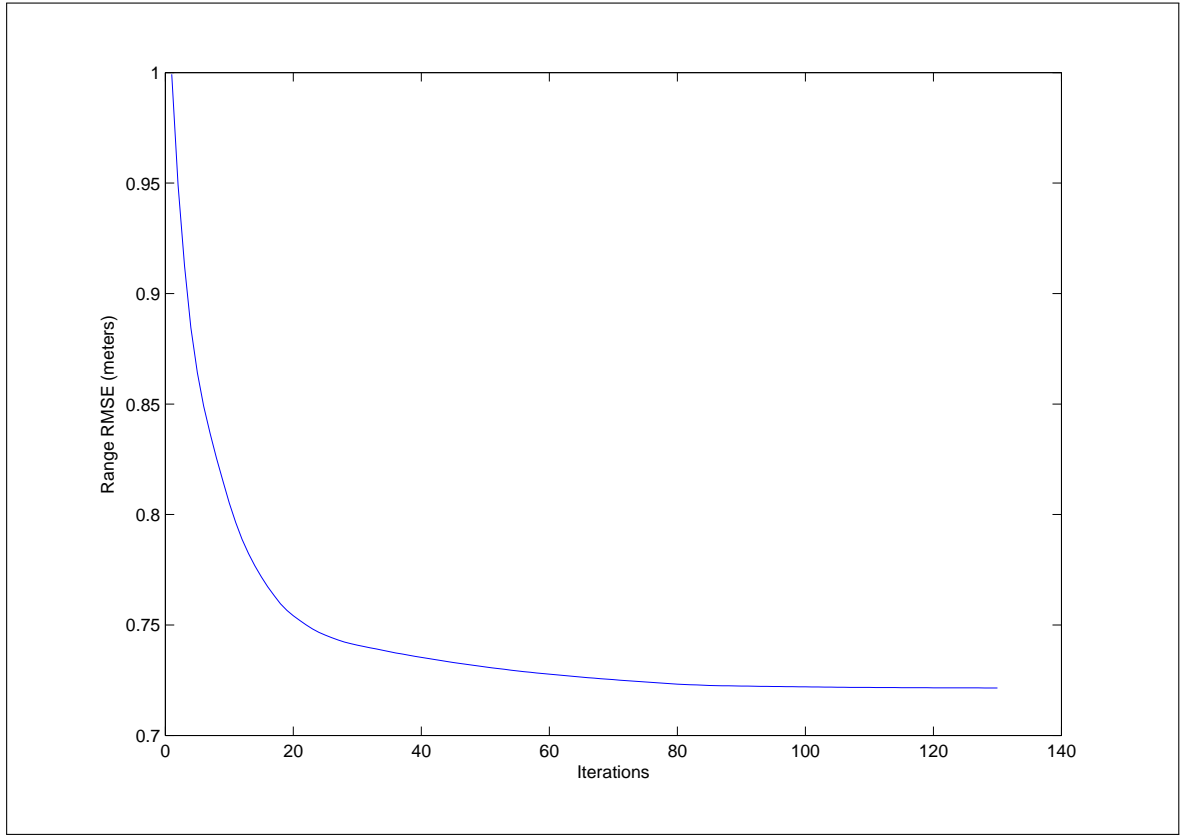


Figure 4.5: Range RMSE vs iterations after applying the proposed algorithm to the measured data. The graph shows the most RMSE reduction occurring between zero and forty iterations. The algorithm reaches convergence after approximately the hundredth iteration.

Table 4.3: Method comparison for the measured data

Method	Range RMSE
Proposed Algorithm	721 mm
Pixel Replication	779 mm
Linear Interpolation	787 mm
Cubic Interpolation	788 mm

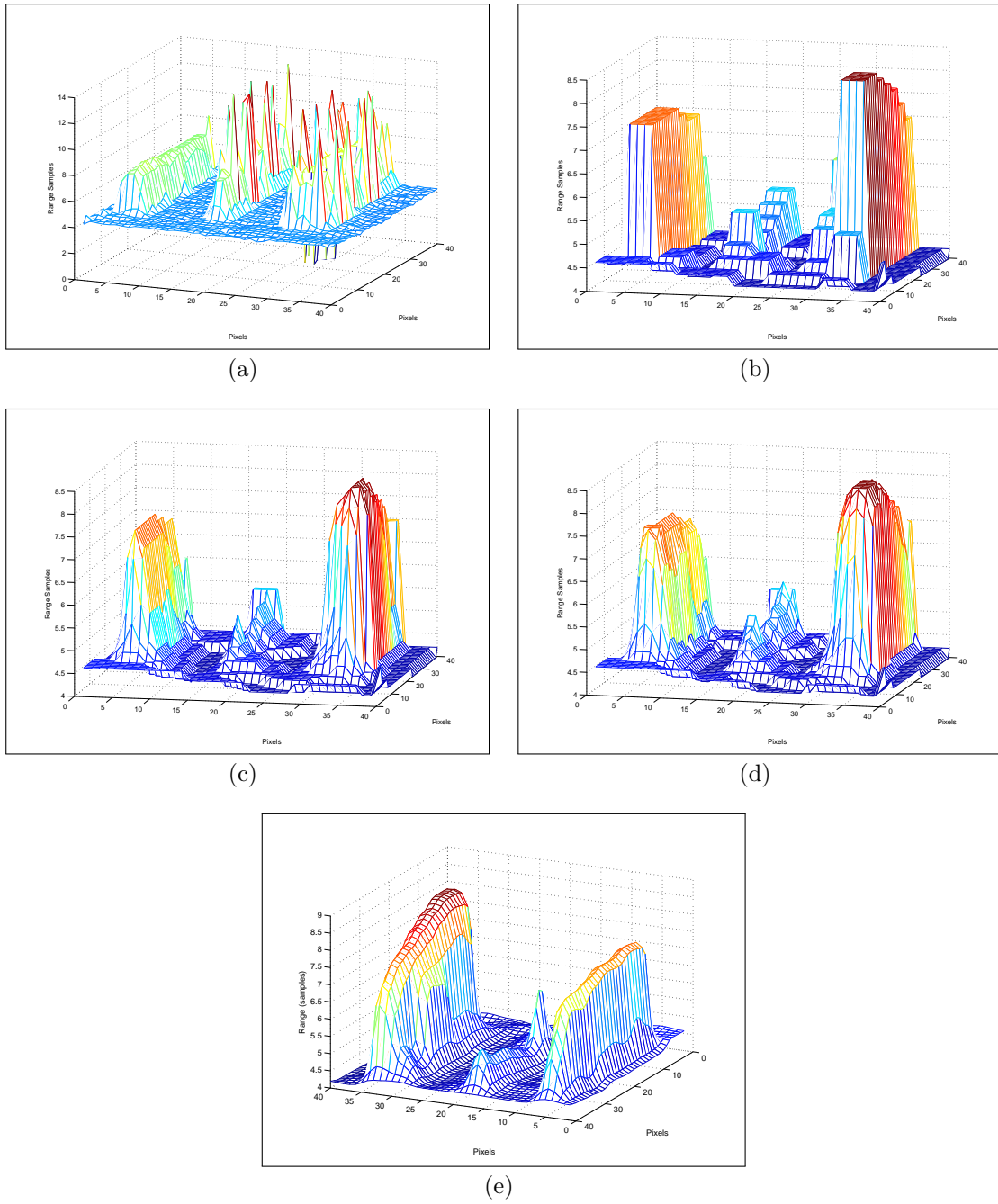


Figure 4.6: (a) 40-by-40 3-D range truth of the measured data. Measured data 40-by-40 3-D estimated ranges: (b) Pixel replication estimated range. (c) Linear estimated range. (d) Cubic estimated range. (e) EM algorithm's estimated range.

## V. Conclusions and Future Work

This section details conclusions that were drawn from the results of this research. Future research potential is also presented here.

### 5.1 Conclusions

This research proves that fusion of 2-D and 3-D LADAR images through EM increases the range accuracy of 3-D images. The combination of 2-D high spatial resolution images and 3-D FLASH LADAR images produces a new LADAR system with improved resolution over current realizable FLASH 3-D sensors. The algorithm's direct solution for the range and bias allows it to be applied to both measured and simulated data, as proved in this research.

Several conditions were used to create three data sets for this research. The results for each data set show the EM solution's range estimation is a vast improvement over both no-processing and interpolation. This case is made clearer with the results shown in the simulated multi-building target (second target), in which the algorithm makes a sixty-five percent improvement over the best interpolation results. The EM solution was created under the assumption that the 2-D and 3-D data was statistically independent, while this was the case for the simulated data it was not for the measured data. In most cases when using two cameras the data and noise will be statistically independent. Given this finding the EM algorithm still was an improvement over interpolation for the measured data. If the data was statistically independent the proposed algorithm would have done better. While the EM solution may be more computationally intensive and require a second 2-D camera, the range accuracy would be a good trade-off given the inaccuracy of interpolation.

The one shot capability the fusion of 2-D and 3-D FLASH LADAR images provides would work as fast or faster than microscanning LADAR systems. Again, LADAR microscanning can involve latency due to the fact of the numerous cubes it needs. The algorithm for fusing 2-D and 3-D LADAR images opens up the possibility of new LADAR capabilities.

## 5.2 *Future Work*

The algorithm proved successful using registered 2-D and 3-D images. Future work involving a registration method built into the algorithm would further develop this type of system as a stand alone system that includes a 2-D camera and 3-D LADAR system. registration is not the only issue involved with using two different cameras. In most cases the cameras do not possess the same sampling, as well as the images from both cameras are uncorrelated. Some type of calibration as well as statistical analysis of the systems would make the algorithm work better and make a stand alone system.

As evidenced in the measured data, noise reduction in 3-D LADAR systems would also make this algorithm work more effectively in range estimation. The measured data was very noisy and contained numerous spikes that if suppressed would allow the algorithm to perform better. Estimating noise may be a possibility to reduce noise in the images. Performing gain variation compensation and enacting a photon counting algorithm would also improve the algorithm with respect to the measured data.

The algorithm only considered a fixed OTF, using blind deconvolution to estimate the OTF would only bolster the performance of the algorithm. The work only considered range and bias estimation, the more estimation built into it the better range accuracy the system would be able to achieve.

Future work involving a comparison of the algorithm to microscanning would prove what the best method of processing LADAR images would be. The comparison should take into account the time it takes to process imagery and range accuracy of each method. Using measured data from LADAR cameras would be a fairer comparison of the two processing types.

## Bibliography

1. Armstrong, Ernest and Richard Richmond. “The Application of Inverse Filters to 3D Microscanning of LADAR Imagery”. *IEEE Aerospace Conf.*, July 2006.
2. Cain, Stephen. “Bayesian-based Fusion of 2-D and 3-D LADAR Imagery”. *2009 IEEE Aerospace Conf.*, 19. October 2009.
3. Dempster, Arthur P., Nan M. Laird, and Donald B. Rubin. “Maximum likelihood from incomplete data via the EM algorithm”. *Royal Stat. Soc. Ser. B*, 39(1), 1977.
4. Goodman, Joseph W. *Fourier Optics*. Roberts & Company, Greenwood Village, CO, 3rd edition, 2005. ISBN 0-9747077-2-4.
5. Haala, Norbert. “Panoramic Scenes for Texture Mapping of 3D City Models”. *Panoramic Photogrammetry Workshop*. February 2005.
6. Krishnaswamy, Kailash. “Ladar-based motion estimation for navigation”. Patent, December 2008. URL <http://www.freepatentsonline.com/7463340.html>.
7. McMahon, Jason R., Richard K. Martin, and Stephen C. Cain. “Three-Dimensional FLASH Laser Radar Range Estimation via Blind Deconvolution”. *J. Appl. Remote Sens.*, 4(043517), 2010.
8. Miklòs, Pòth. “Image Interpolation Techniques”. *2nd Siberian-Hungarian Joint Symposium On Intelligent Systems*. October 2004.
9. Richardson, Hadley W. “Bayesian-Based Iterative Method of Image Restoration”. *J. Opt. Soc. Am.*, 62:55–59, January 1972.
10. Richmond, Richard and Stephen Cain. *Direct-Detection LADAR Systems*. SPIE, Bellingham, WA, 2010. ISBN 9780819480729.
11. Seal, Michael D. *Nonlinear time-variant response in an avalanche photodiode array based laser detection and ranging system*. Master’s thesis, Air Force Institute of Technology, 2007.
12. Shepp, L. A. and Y. Vardi. “Maximum-likelihood reconstruction for emission tomography”. *IEEE Transactions on Medical Imaging*, MI-1(2):113–122, October 1982.
13. Vanbebber, Craig and Everett Tackett. “Lockheed Martin, Netfires LLC Demonstrate Dual-Mode Laser Radar - Semi-Active Laser Sensor Capability for Target Designation, Acquisition and Tracking”. Press Release, January 2007.

# REPORT DOCUMENTATION PAGE

*Form Approved*  
*OMB No. 0704-0188*

The public reporting burden for this collection of information is estimated to average 1 hour per response, including the time for reviewing instructions, searching existing data sources, gathering and maintaining the data needed, and completing and reviewing the collection of information. Send comments regarding this burden estimate or any other aspect of this collection of information, including suggestions for reducing this burden to Department of Defense, Washington Headquarters Services, Directorate for Information Operations and Reports (0704-0188), 1215 Jefferson Davis Highway, Suite 1204, Arlington, VA 22202-4302. Respondents should be aware that notwithstanding any other provision of law, no person shall be subject to any penalty for failing to comply with a collection of information if it does not display a currently valid OMB control number. **PLEASE DO NOT RETURN YOUR FORM TO THE ABOVE ADDRESS.**

<b>1. REPORT DATE (DD-MM-YYYY)</b> 24-03-2011		<b>2. REPORT TYPE</b> Master's Thesis		<b>3. DATES COVERED (From — To)</b> May 2009 — Mar 2011	
<b>4. TITLE AND SUBTITLE</b>  A Statistical Approach to Fusing 2-D and 3-D LADAR Systems				<b>5a. CONTRACT NUMBER</b>	
				<b>5b. GRANT NUMBER</b>	
				<b>5c. PROGRAM ELEMENT NUMBER</b>	
				<b>5d. PROJECT NUMBER</b>	
<b>6. AUTHOR(S)</b>  Paul Dolce, Captain, USAF				<b>5e. TASK NUMBER</b>	
				<b>5f. WORK UNIT NUMBER</b>	
				<b>8. PERFORMING ORGANIZATION REPORT NUMBER</b>  AFIT/GE/ENG/11-09	
<b>7. PERFORMING ORGANIZATION NAME(S) AND ADDRESS(ES)</b> Air Force Institute of Technology Graduate School of Engineering and Management (AFIT/EN) 2950 Hobson Way WPAFB OH 45433-7765				<b>10. SPONSOR/MONITOR'S ACRONYM(S)</b>  AFRL/RWGSL	
<b>9. SPONSORING / MONITORING AGENCY NAME(S) AND ADDRESS(ES)</b> David G. Edwards Air Force Research Lab, AFMC 101 W. Eglin Blvd, Suite 219, Bldg 13 Eglin AFB, FL, 32542-5429 DSN: 872-4617 David.Edwards@eglin.af.mil					
<b>12. DISTRIBUTION / AVAILABILITY STATEMENT</b>  APPROVED FOR PUBLIC RELEASE; DISTRIBUTION UNLIMITED. This material is declared a work of the U.S. Government and is not subject to copyright protection in the United States.				<b>11. SPONSOR/MONITOR'S REPORT NUMBER(S)</b>	
<b>13. SUPPLEMENTARY NOTES</b>					
<b>14. ABSTRACT</b>  LADAR (LAsER Detection and Ranging) systems can be used to provide 2-D and 3-D images of scenes. Generally, 2-D images possess superior spatial resolution but without range data due to the density of their focal plane arrays. A 3-D LADAR system can produce range to target data at each pixel, but lacks the 2-D system's superior spatial resolution. The 3-D system is limited by its hardware, specifically its imaging array. Currently developers are investigating ways to change the pixel size in the 3-D LADAR imaging array, but the costs of this research is quite expensive and technically robust. It is the goal of this work to develop an Expectation Maximization approach to estimate both 3-D LADAR range and the bias associated with a 3-D LADAR system. The algorithm developed demonstrates both spatial and range resolution improvement over standard interpolation techniques using both real and simulated 3-D and 2-D LADAR data.					
<b>15. SUBJECT TERMS</b>  3-D LADAR, Range Estimation, Expectation Maximization					
<b>16. SECURITY CLASSIFICATION OF:</b>			<b>17. LIMITATION OF ABSTRACT</b>	<b>18. NUMBER OF PAGES</b>	<b>19a. NAME OF RESPONSIBLE PERSON</b> Stephen C. Cain, Civ, USAF, (ENG)
a. REPORT	b. ABSTRACT	c. THIS PAGE			<b>19b. TELEPHONE NUMBER (include area code)</b> (937) 255-3636, x4716; Stephen.cain@afit.edu
U	U	U	UU	53	